

RHEINISCH-WESTFÄLISCHE TECHNISCHE HOCHSCHULE AACHEN

Simulation and Optimization of the Spin Coherence Time of Protons in a Prototype EDM Ring

BY

MAXIMILIAN VITZ

MASTER THESIS

SUBMITTED TO THE

FACULTY FOR MATHEMATICS, COMPUTER SCIENCE AND NATURAL SCIENCE

OF THE RWTH AACHEN UNIVERSITY

IN OCTOBER 2020

CARRIED OUT AT THE

III. PHYSIKALISCHEN INSTITUT B

UNDER

PROF. DR. ANDREAS LEHRACH

Abstract

Simulation and Optimization of the Spin Coherence Time of Protons in a Prototype EDM Ring

The matter-antimatter asymmetry in the Universe might be understood by investigating the Electric Dipole Moment (EDM) of elementary charged particles. A permanent EDM of a subatomic particle violates time reversal and parity symmetry at the same time and would be a strong indication for physics beyond the Standard Model. The Jülich Electric Dipole moment Investigations (JEDI) collaboration is carrying out a project for the direct measurement of a permanent EDM of protons and deuterons. For this reason a dedicated electrostatic storage ring is in development. As an intermediate step a prototype ring is being developed to demonstrate sufficient beam lifetime and Spin Coherence Time (SCT) in a pure electrostatic ring as well as in a storage ring with combined electric and magnetic bending elements. The scope of this thesis is the simulation of a prototype ring with combined electric and magnetic bending elements and the investigation of the influence of chromaticity on the SCT. It will be shown that a vanishing horizontal and vertical chromaticity does not cause the maximal SCT, as one might expect from initial theoretical considerations. The optimal sextupole settings have to be determined individually for each working point as will be demonstrated within this thesis.

Simulation und Optimierung der Spin Kohärenz Zeit von Protonen in einen Prototype EDM Ring

Die Asymmetrie zwischen Materie und Antimaterie im Universum könnte durch die Untersuchung des Elektrischen Dipole Momentes (EDM) von elementar geladenen Teilchen verstanden werden. Das permanente EDM eines subatomaren Teilchens verletzt die Zeit Umkehr und Parität gleichzeitig und wäre ein Anzeichen für Physik jenseits des Standard Models. Die Jülich Electric Dipole moment Investigations (JEDI) Collaboration führt ein Projekt zur direkten Messung des permanenten EDMs von Protonen and Deuteronen durch. Aus diesem Grund ist ein geeigneter elektrostatischer Speicherring in Entwicklung. Als Zwischenschritt wird ein Prototype entwickelt um ausreichende Lebenszeit des Teilchenstrahls sowie Spin Kohärenz Zeit (SCT) in einem rein elektrischen Ring und in einem Ring mit kombinierten elektrischen und magnetischen Dipolen zu demonstrieren. Ziel dieser Arbeit ist die Simulation eines solchen Prototype Ringes und mithilfe dieser den Einfluss der Chromatizität auf die SCT zu untersuchen. Es wird gezeigt werden, dass eine verschwindende horizontale und vertikale Chromatizität nicht die maximale SCT verursacht, wie man durch anfängliche theoretische Überlegungen erwarten würde. Diese Arbeit zeigt, dass die optimalen Sextupole Einstellungen individuell für jeden Arbeitspunkt bestimmt werden müssen.

Contents

1	Introduction	1
2	Scientific Motivation	3
2.1	Matter-Antimatter Asymmetry	3
2.2	Electric Dipole Moment	4
3	Theoretical Background	5
3.1	Coordinate System	5
3.2	Beam Dynamics	6
3.2.1	Transverse Beam Dynamics	6
3.2.2	Longitudinal Beam Dynamics	13
3.3	Spin Dynamics	17
3.3.1	Spin Formalism	17
3.3.2	Spin Motion	17
3.4	Principle of Electric Dipole Moment Measurement	19
3.4.1	Frozen Spin Method	21
3.4.2	Spin Tune Spread and Spin Coherence Time	22
3.4.3	Depolarizing Spin Resonances	23
4	Prototype EDM Storage Ring	25
4.1	Project Overview	25
4.2	Design	26
4.3	Implementation into Bmad	28
4.4	Benchmarking the Model	30
4.4.1	Definition of Phase Space	30
4.4.2	Investigation of numerical noise	30
4.4.3	Dipole fields and frozen spin	33
4.4.4	Phase Space Ellipse	35
5	Optical Flexibility of the Lattice	37
5.1	The Working Point	37
5.2	The Chromaticity	40
5.2.1	Discussion of chromaticity for small rings	42
5.2.2	Discussion of chromaticity for large rings	43
5.3	Chromaticity Correction	45

6 Investigation of Spin Motion	49
6.1 Preparation	49
6.1.1 Chosen Working Point	49
6.1.2 Initial Beam Parameter	51
6.2 Variation of vertical Chromaticity	55
7 Summary and Outlook	63
8 Appendix	i
List of Figures	iii
List of Tables	v
Bibliography	vii

1 Introduction

The object of physics is the explanation of nature in equations and mathematical models. The most known model is the Standard Model (SM) of particle physics. It is an overall accepted model which describes elementary particles and their interactions. The SM was confirmed by many experimental observations and also provided predictions which lead to many new discoveries. Despite its success there are also fields in modern physics where the SM lacks an explanation. One of these fields is the dominance of matter over antimatter in the known part of the Universe. Although SM predicts such an asymmetry, the observed asymmetry is magnitudes higher than the SM prediction. One possible explanation for this observation is the disappearance of antimatter during the baryogenesis of Universe. This would require a violation of fundamental symmetries. A new particle property called the EDM can explain this violation process. Its influence is strongly suppressed in the SM [1].

The JEDI collaboration at the Institut für Kernphysik in the Forschungszentrum Jülich is investigating the EDM of charged particles. It is planned to perform a direct measurement of the EDM of protons and deuterons using a storage ring. The general idea is to store a bunch of particles with initial longitudinal spin polarization and measure the vertical polarization build-up with a polarimeter. Such an experiment is currently performed at the Cooler Synchrotron (COSY) in Jülich and should deliver first measurements on the deuteron EDM magnitude. As the EDM is coupled to the particles spin it would lead to a build-up of vertical polarization by radial electric fields. To increase the magnitude of these fields and to reduce systematic uncertainties a new purely electrostatic storage ring is in development. Before building such a dedicated ring the feasibility of such an EDM measurement in a storage ring has to be shown, technical issues have to be clarified and simulations have to be performed. For this reason a prototype ring is planned. The prototype ring should be much smaller than the final ring and operate in two different modes. The first mode should be a pure electric mode and the second should combine electric and magnetic fields. In the end this prototype should demonstrate sufficient beam lifetime and SCT, which indicates how long the spin remains aligned with the particle's momentum, and work as a proof of principle experiment [2][3].

The aim of this thesis is to simulate the beam and spin motion in the prototype EDM storage ring (PTR). The simulation should show first results of the SCT in dependency of the chromaticity configuration in the ring. Additionally, the variability of the betatron tunes and other ring properties are investigated. The software library Bmad is used as a

tool to simulate an idealized model of the prototype ring.

This thesis has the following structure: Chapter 2 gives a short scientific motivation for an EDM measurement. There, it will also be explained what an EDM is and why it may be so important for modern physics. The theoretical background for a measurement of an EDM in a storage ring is provided in chapter 3. In particular the beam and spin motion in a storage ring are discussed. In chapter 4 the properties of the PTR are explained and its implementation into the simulation tool Bmad is shown. Possible working points by variation of the quadrupoles are examined in chapter 5. The natural chromaticity of the individual working points and its correction through sextupoles is also discussed. Chapter 6 shows first simulation results on the SCT and the spin tune spread for one working point with different chromaticity configurations. Chapter 7 summaries the results of this thesis and gives an outlook on the future of this project.

2 Scientific Motivation

2.1 Matter-Antimatter Asymmetry

The amount of matter in the Universe is exceeding the amount of antimatter by far. This is a surprising fact, as one expects that after the big bang the Universe consisted of equal amounts of matter and antimatter. The asymmetries magnitude has been measured by a series of measurements of cosmic microwave background radiation and summarized in the baryon-to-photon density ratio [4][5]:

$$\eta = \frac{n_b - n_{\bar{b}}}{n_\gamma} = (6.08 \pm 0.09) \cdot 10^{-10}. \quad (2.1)$$

The ratio is depending on the baryon density n_b and anti-baryon density $n_{\bar{b}}$ as well as the photon density n_γ . The SM of particle physics also describes such an asymmetry, although its prediction is about eight orders of magnitude smaller than the observed ratio [6]:

$$\frac{n_b}{n_\gamma} = \frac{n_{\bar{b}}}{n_\gamma} \approx 10^{-18}. \quad (2.2)$$

The measured asymmetry may be explained by an asymmetric annihilation process of matter and antimatter which is resulting in the measured excess of matter. To realize such an annihilation process three conditions formulated by Sakharov need to be fulfilled [7]:

- **Violation of Baryon number:** The annihilation process has to violate the baryon number conservation, otherwise there is no possible way out of an initial baryon charge number of $B=0$.
- **Violation of C and CP:** It has to violate C and CP so that the rates of baryon production and antibaryon production are different.
- **No thermal equilibrium:** The annihilation process had to take place during a stage of non-equilibrium in Universe, since otherwise CPT-symmetry would assure that $\langle B \rangle = 0$ holds in average.

The violation of the baryon number can be explained within the SM. However, the C and

CP violation in the SM is too small to explain the measured asymmetry. Therefore, there have to be other sources of C and CP violation. This is one of the few existing indicators that there might be physics beyond the Standard Model [4].

2.2 Electric Dipole Moment

One additional source of CP violation could be the EDM \vec{d} which is defined as a permanent separation of charges inside a particle. Similar to the Magnetic Dipole Moment (MDM) $\vec{\mu}$ it is a fundamental property of a particle and aligned parallel or anti-parallel to its spin \vec{s} [8]:

$$\vec{d} = \frac{\eta}{2} \frac{e}{m} \vec{s} \quad (2.3)$$

$$\vec{\mu} = \frac{g}{2} \frac{e}{m} \vec{s}. \quad (2.4)$$

In these equations e denotes the elementary charge of a particle and m is its mass. The parameters g and η are dimensionless scaling factors for the different dipole moments. Considering the MDM and the EDM of a particle it leads to the following Hamiltonian [9]:

$$H = -\vec{\mu} \cdot \vec{B} - \vec{d} \cdot \vec{E}. \quad (2.5)$$

The external electric field is described with \vec{E} and the corresponding magnetic field with \vec{B} . The parity and time reversal symmetries get violated by applying their transformation rule to this Hamiltonian. Violating P and T also implies CP violation assuming that CPT symmetry is conserved [4].

The SM predicts an EDM although its magnitude is exceedingly small. In case of nucleons the calculations of SM lead to a magnitude of $10^{-33} \text{ e}\cdot\text{cm} < d_N < 10^{-31} \text{ e}\cdot\text{cm}$. Measuring an EDM at a higher limit than the SM prediction would increase CP violation and could explain the measured asymmetry between matter and antimatter. Up to now only upper limits for an EDM were found but no EDM signal itself. It is not sufficient to measure only the EDM of one particle, e.g. the neutron, because the source of the EDM cannot be found this way. The results for upper limits of different particles are summarized in table (2.1) [10][11]:

Table 2.1: Current upper limits of EDM searches.

Particle	Neutron	Proton	Electron
$ d $	$2.9 \cdot 10^{-26} \text{ e cm}$ (90% C. L.) [12]	$7.9 \cdot 10^{-25} \text{ e cm}$ (95% C. L.) [13]	$8.7 \cdot 10^{-29} \text{ e cm}$ (90% C. L.) [14]

3 Theoretical Background

The EDM of elementary charged particles can be investigated via storage rings. The knowledge of beam and spin dynamics is essential for such an investigation. The following chapter will present basic knowledge of accelerators physics. Also methods for EDM measurements in storage rings will be discussed.

3.1 Coordinate System

In a first step a coordinate system for storage rings has to be defined. As the dimensions of a beam are very small in comparison to the whole storage ring the particle coordinates are describe in relation to its ideal trajectory around the storage ring. The individual particle is described in a co-moving coordinate system which has its origin on the ideal orbit. The horizontal discrepancy of the reference particles to the described particle is marked x , the vertical with y and the longitudinal with z . The co-moving coordinate system is illustrated in figure (3.1). The transformation of the basis vectors from one place s to another s' is defined by a simple rotation [15][16]:

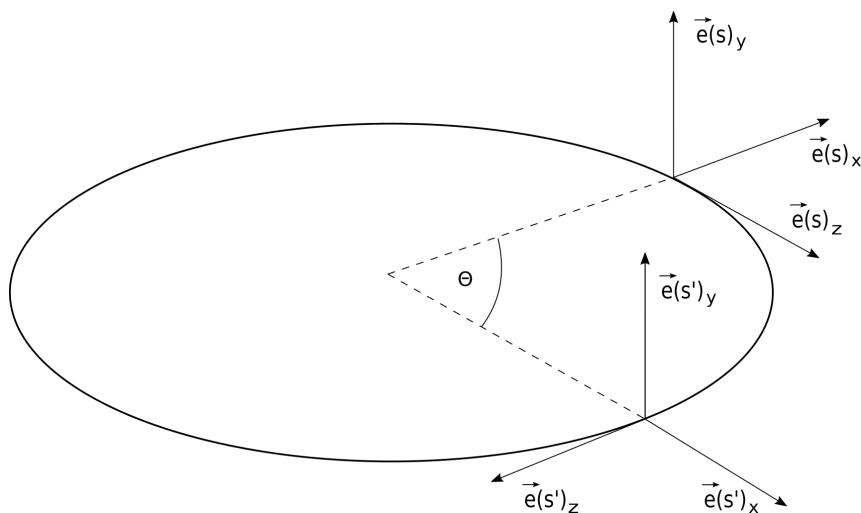


Figure 3.1: Co-moving coordinate system with the Cartesian coordinates \vec{e}_x , \vec{e}_y and \vec{e}_z at two position s and s' inside the storage ring. The parameter θ denotes the angular between the two position s and s' . The origin of the coordinate system is always the particle on the ideal trajectory which is called the reference particle. Inspired by [15].

$$\vec{e}(s')_x = \cos(\theta) \cdot \vec{e}(s)_x + \sin(\theta) \cdot \vec{e}(s)_z \quad (3.1)$$

$$\vec{e}(s')_y = \vec{e}(s)_y \quad (3.2)$$

$$\vec{e}(s')_z = -\sin(\theta) \cdot \vec{e}(s)_x + \cos(\theta) \cdot \vec{e}(s)_z. \quad (3.3)$$

3.2 Beam Dynamics

A particle beam consists of a multitude of particles. The motion of each of these particles can be described relative to the reference particle. In addition to the previously discussed physical offsets in the Cartesian coordinates there are corresponding offsets in the momenta. The spatial offsets and the momentum offsets form a six dimensional phase space. Differential equations can be derived for this six dimensional phase space to describe the motion of the single particle in the storage ring [15][16].

3.2.1 Transverse Beam Dynamics

The transverse phase space is defined as the plane spanned between horizontal $\vec{e}(s)_x$ and vertical $\vec{e}(s)_y$ coordinates. In this section the equation of motion in this plane will be discussed. For this purpose a storage ring design with static transversal magnetic fields up to linear order will be considered.

Static Magnetic Field

A static transversal magnetic field B is needed to keep the reference particle with momentum p on its circular trajectory through the accelerator. The basic equation describing the necessary magnetic field comes from setting the Lorentz force equal to the centrifugal force. Since the transverse beam dimensions are small compared to the bending radius R of the particle trajectory, one can develop the magnetic field for small deviations from the ideal trajectory which results in [15][16]:

$$\frac{1}{R(x, y, z)} = \frac{e}{p} B_y(x, y, z) \quad (3.4)$$

$$\begin{aligned}
\Rightarrow \frac{e}{p} B_y(x) &= \frac{e}{p} B_{y,0} + \frac{e}{p} \frac{dB_y}{dx} x + \frac{1}{2!} \frac{e}{p} \frac{d^2 B_y}{dx^2} x^2 + \dots \\
&= \frac{1}{R} + kx + \frac{1}{2!} mx^2 + \dots \\
&\quad \text{Dipole} \qquad \qquad \text{Quadrupole} \qquad \qquad \text{Sextupole}
\end{aligned}$$

One obtains a description which shows the impact of different magnet configurations as the dipole, quadrupole and the sextupole. Also higher order configurations can be considered in this way. The quantities k and m represent the strengths of the quadrupole and the sextupole.

Hill's Differential Equation

Hill's differential equation is the fundamental basis to describe the particle motion in the transverse phase space. It considers field components up to linear order which include dipoles and quadrupoles but no sextupoles. With this approach the horizontal and vertical motion decouple and behave independently from each other as can be described by [15]:

$$x''(s) + \left(\frac{1}{R^2(s)} - k(s) \right) x(s) = \frac{1}{R(s)} \frac{\Delta p}{p} \quad (3.5)$$

$$z''(s) + k(s)z(s) = 0. \quad (3.6)$$

In equation (3.6) the quantities $x''(s)$ and $z''(s)$ denotes the second derivation after the quantity s . An other s depended quantity is the bending radius $R(s)$ which only contributes at places where dipole fields are present. The same applies to $k(s)$ which is the strength of a quadrupole and only arises in quadrupole fields. Its sign is varying between equation (3.5) and (3.6). The reason for that behavior is that a quadrupole can only be focusing in one direction but defocuses in the other. The definition chosen here is that a positive k value is describing a horizontally defocusing quadrupole. A momentum deviation of a particle in relation to the reference particle is described by $\Delta p/p$. The momentum deviation is only present in equation (3.5) and is sketching that longitudinal phase space and horizontal phase space are coupled [15].

Dispersion

As shown in equation (3.5) the horizontal motion of a particle is influenced by its momentum deviation compared to the reference particle. The particle motion inside a dipole where no quadrupole field is present can therefore be described by [15]:

$$x''(s) + \frac{1}{R^2(s)}x(s) = \frac{1}{R(s)}\frac{\Delta p}{p}. \quad (3.7)$$

Equation (3.7) is an inhomogeneous differential equation and therefore its solution is a combination of a homogeneous part $x(s)$ and an inhomogeneous part $x_D(s)$. The homogeneous solution shows the evolution of the phase space coordinates of an observed particle if no deviation in momentum to the reference particle would be present. The inhomogeneous solution is shifting the motion to dispersive trajectories described by [15]:

$$x_g(s) = x(s) + x_D(s) = x(s) + D(s)\frac{\Delta p}{p}. \quad (3.8)$$

The property $D(s)$ which is describing the dispersive trajectory $x_D(s)$ is called dispersion. It is directly connected to the curvature $R(s)$ as it occurs due to a mismatch of bending power of the dipoles in presence of a momentum deviation [15].

Particle Emittance

Without considering a momentum offset equation (3.5) becomes a differential equation very similar to equation (3.6). Both equations differ from the differential equation of the harmonic oscillator by the s dependence of k , which would be constant in case of a harmonic oscillator. Nevertheless a similar approach to solve the differential equation can be used. The differential equation and its solution is exemplary sketched for the horizontal phase space in the following equations [15]:

$$x''(s) - k(s)x(s) = 0 \quad (3.9)$$

$$\Rightarrow x(s) = \sqrt{\epsilon}\sqrt{\beta(s)}\cos(\psi(s) + \phi). \quad (3.10)$$

The combination of $\sqrt{\epsilon}\sqrt{\beta(s)}$ forms a location-dependent amplitude of the oscillation. Here the parameter ϵ is a constant for an individual particle and named one-particle emittance. The so called β -function is an optical parameter which is varying with the beam focusing and therefore depends on s . Together with the phase advance $\psi(s)$ and the phase ϕ these quantities describe the motion of an individual particle in the horizontal phase space. The phase advance is directly connected to the β -function via [15]:

$$\psi(s) = \int_0^s \frac{1}{\beta(s')}ds'. \quad (3.11)$$

Phase Space Ellipse

The importance of the β -function is also shown by the fact that it defines two additional system parameters α and γ . These three quantities together are called optical functions [15]:

$$\alpha(s) = -\frac{\left(\frac{d\beta(s)}{ds}\right)}{2} \quad (3.12)$$

$$\gamma(s) = \frac{1 + \alpha^2(s)}{\beta(s)}. \quad (3.13)$$

The optical functions can be derived for the horizontal and the vertical phase space. With the help of these system parameters and the equation for the orbital movement in the horizontal plane $x(s)$ and vertical plane $y(s)$ as well as their derivation $x'(s)$ and $y'(s)$ one obtains the so called phase space ellipse. It is described exemplary for the horizontal phase space in equation (3.14) and sketched in figure (3.2). The vertical phase space behaves identically. The form and orientation of the ellipse depends on the β -function. Its area is defined by the Courant-Snyder-Invariant constant ϵ [15].

$$\gamma(s)x^2(s) + 2\alpha(s)x(s)x'(s) + \beta(s)x'^2(s) = \epsilon \quad (3.14)$$

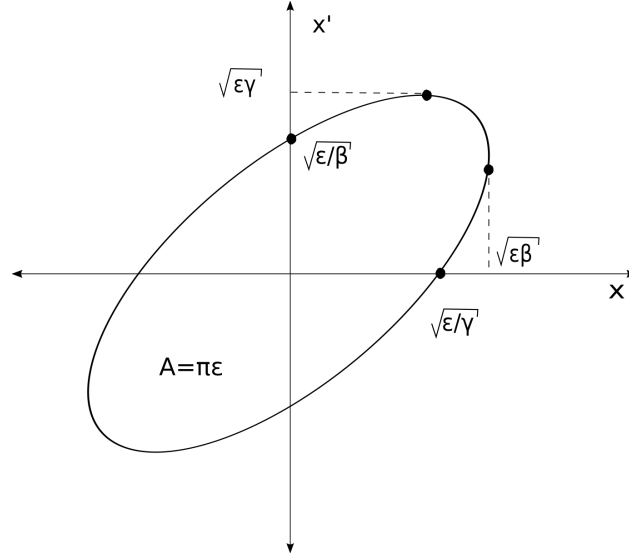


Figure 3.2: Phase space ellipse for horizontal phase space at an arbitrary position inside the storage ring. The x-axis shows the horizontal offset x of a particle relative to the reference particle and the y-axis the derivation of the horizontal offset x' . The quantities α , β and γ are the optical functions of the horizontal phase space. The area A of the ellipse is defined by the Courant-Snyder-Invariant ϵ . Inspired by [15].

Beam Emittance

In a beam, there are many particles that move with different amplitudes, so that the areas of the phase ellipses are also different. Thus, a mean emittance must be assigned to the beam. To derive a definition of the emittance of a particle beam, one considers an equilibrium distribution of all particles, which is constant in time. This can be described by a two dimensional Gaussian distribution in the transversal phase space in an idealized case [15]:

$$\rho(x, y) = \frac{Ne}{2\pi\sigma_x\sigma_y} \exp\left(-\frac{x}{2\sigma_x^2} - \frac{y}{2\sigma_y^2}\right). \quad (3.15)$$

In this equation N shows the number of particles while σ_x and σ_y represent the standard deviation of the Gaussian distribution. The standard deviation is connected to the beam emittance ϵ_{beam} via [15]:

$$\sigma_{beam_{x,y}}(s) = \sqrt{\epsilon_{beam_{x,y}} \cdot \beta(s)} \quad (3.16)$$

$$\epsilon_{beam_{x,y}} = \frac{\sigma_{beam_{x,y}}^2(s)}{\beta(s)} \quad (3.17)$$

Betatron Tune

As the quadrupoles are used for beam focusing they also define the number of betatron oscillations a particle performs during one turn in a storage ring. This is described by the β -function. The number of betatron oscillations during one turn is called betatron tune. It needs to be calculated for the horizontal and the vertical phase space separately for an uncoupled motion which is shown in equation (3.18), where i denotes the horizontal and vertical phase space respectively [15]:

$$Q_i = \frac{1}{2\pi} \oint \frac{ds}{\beta_i(s)}. \quad (3.18)$$

The combination of horizontal and vertical betatron tune defines the working point of a storage ring. If the working point fulfills a so called resonance condition the amplitude of a particle is growing massively which lead to a loss of the particle. A resonance condition is build up on the incident that a particle is facing the same storage ring structure in every turn. In result the same forces are acting on the particle periodically. If a resonance condition is fulfilled these kicks coherently add up from turn to turn and push the observed

particle away from the design orbit until the bending dipoles and quadrupoles are not able to keep the particle inside the storage ring any more. An equation which defines the resonance condition criteria is shown below [15]:

$$m \cdot Q_x + n \cdot Q_y = p \quad \text{with} \quad m, n, p \in \mathbb{Z}. \quad (3.19)$$

Here the integer parameter m and n define the order of a resonance which is just $|m| + |n|$. To avoid losing particles due to this betatron resonances the working point has to be chosen far from any low order resonance as these are stronger than high order resonances. A reasonable working point can be found using a tune diagram which is sketched in figure (3.3) [15].

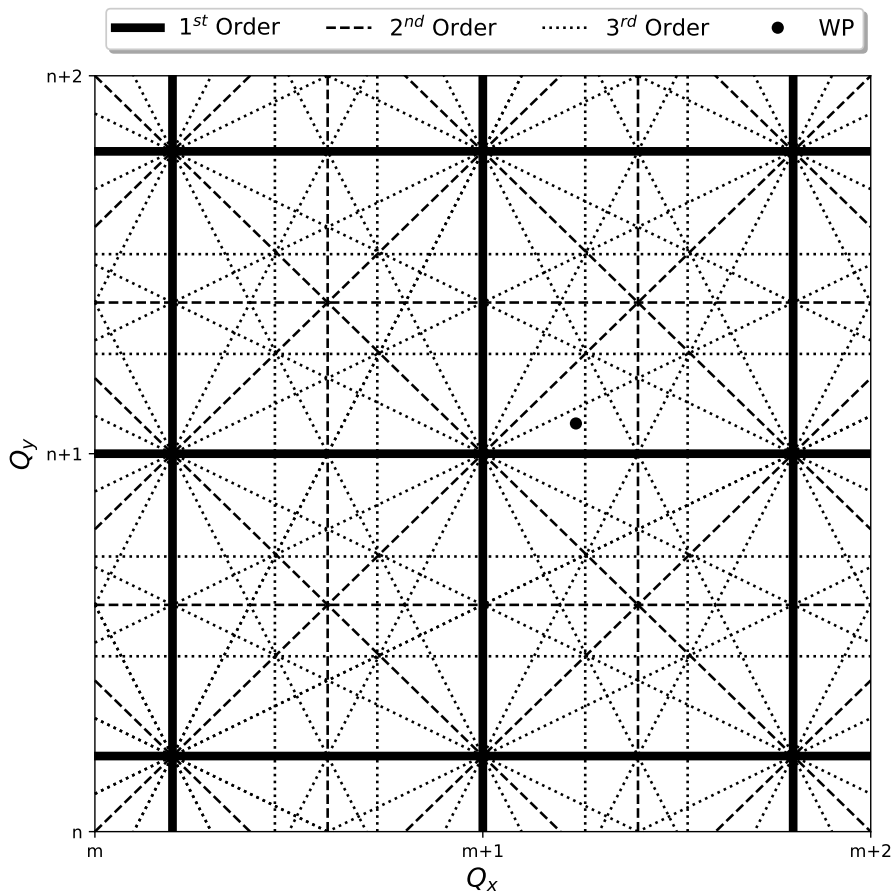


Figure 3.3: Tune diagram with betatron resonances up to third order. The x-axis shows the horizontal betatron tune Q_x and the y-axis the vertical betatron tune Q_y . The integers m and n define the order of the resonance via $|m| + |n|$. Inspired by [15].

Chromaticity

As the optics of a storage ring is designed for the reference particle it is important to know how the optics is changing if a particle's momentum deviates from the momentum of the reference particle. The quantity which is describing the shift of the working point ΔQ_i for a particle offset $\Delta p/p$ is called chromaticity and defined in equation (3.20) [15]:

$$\xi_i := \frac{\Delta Q_i}{\Delta p/p}. \quad (3.20)$$

In case of a large storage ring with strong focusing the contribution of the quadrupoles to the chromaticity becomes dominant. Large is meant in the sense that the bending radius is much larger than the ring dispersion. Strong focusing denotes the fact that quadrupoles with strong fields and alternating gradients are used. The impact of the quadrupoles on the chromaticity is then described by the following equation [15]:

$$\Delta Q_i = \frac{1}{4\pi} \oint \frac{\Delta p}{p} k(s) \beta_i(s) ds. \quad (3.21)$$

Therefore the chromaticity in this case just depends on the strength of the quadrupoles and the magnitude of the β -function at the quadrupoles location. Sextupoles, placed on areas with non vanishing dispersion, are used to manipulate the chromaticity as they generate local quadrupole components depending on the radial position of the particle when passing through the sextupole. Sextupoles do not belong to the linear beam optics any more. A sketch of their operation principle is shown in figure (3.4) and their impact on the chromaticity is given by [15]:

$$\Delta Q_i = \frac{1}{4\pi} \oint \frac{\Delta p}{p} m(s) D(s) ds. \quad (3.22)$$

The final chromaticity of a large ring is a combination of the natural chromaticity of the ring induced by the quadrupoles and the chromaticity correction by the sextupoles. Additionally there are also sextupole components of the dipole and quadrupole magnets. Their strength depends on the excitation of the magnets. However, this simple assumption is no longer valid if one assumes a small storage ring. This is discussed in section (5.2.1) [15].

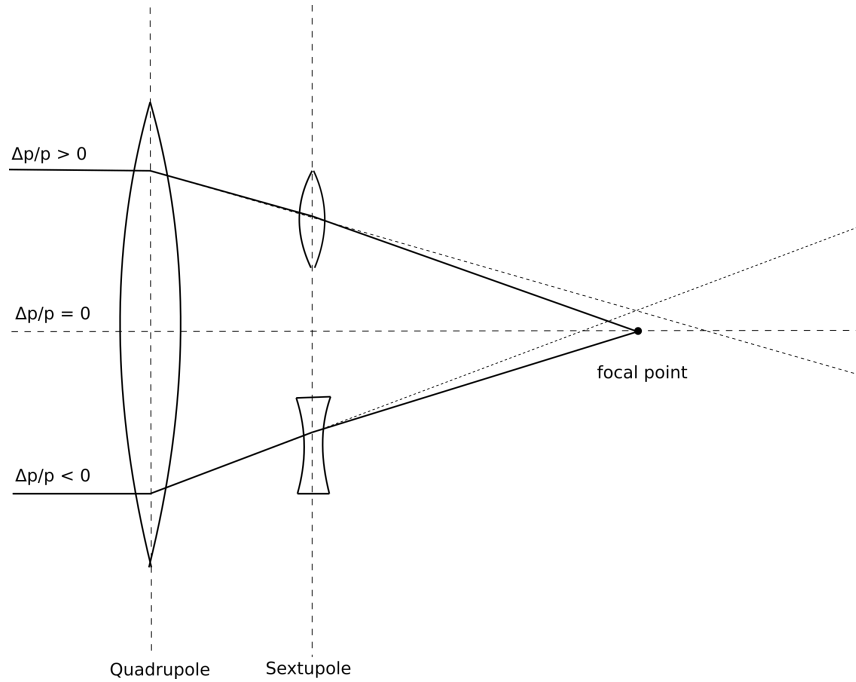


Figure 3.4: Sketch of the principle of chromaticity correction by sextupoles. Sextupoles generate a local quadrupole component depending on the radial position of the particle. In dispersive regions, they can correct for chromatic effects induced by quadrupoles. Inspired by [15].

3.2.2 Longitudinal Beam Dynamics

Path Lengthening

So far only the transverse motion is described. In the longitudinal phase space there are also effects induced by the deviation of the momentum to the reference particle. One of these effects is called path lengthening of off-momentum particles. As the offset particle does not follow the design path any more it either travels more or less distance than the reference particle during one turn inside the storage ring. The quantity which is describing the path lengthening ΔC in relation to the circumference C and the momentum offset is called the momentum compaction factor α_0 [15]:

$$\frac{\Delta C}{C_0} = \alpha_0 \frac{\Delta p}{p}. \quad (3.23)$$

It can also be derived from the fact that the main contribution to its magnitude is coming from the bending dipoles. In quadrupoles path lengthening effects can be neglected as they only occur as higher order effects. This leads to a theoretical description of the momentum compaction factor [15]:

$$\alpha_0 = \frac{1}{C_0} \oint \frac{D(s)}{R(s)} ds. \quad (3.24)$$

The momentum compaction factor α_0 is also the critical parameter which decides which time difference ΔT an offset particle needs for one revolution inside the storage ring relative to the reference particle revolution time T [15]:

$$\frac{\Delta T}{T} = \left(\alpha_0 - \frac{1}{\gamma^2} \right) \frac{\Delta p}{p}. \quad (3.25)$$

As the relation of α_0 and the particle's energy becomes important a new quantity is introduced. This quantity is called transition energy γ_t and can be directly derived from the momentum compaction factor α_0 [15]:

$$\gamma_t = \frac{1}{\sqrt{\alpha_0}} \iff \alpha_0 = \frac{1}{\gamma_t^2}. \quad (3.26)$$

In case the particle's energy γ is below transition energy γ_t , a particle with more momentum than the reference particle ($\Delta p/p > 0$) needs less time for one revolution inside the storage ring than the reference particle. The reverse applies to a particle with less momentum than the reference particle ($\Delta p/p < 0$). If the particle's energy is shifted above transition energy a particle with more momentum than the reference particle ($\Delta p/p > 0$) needs more time for one revolution inside the storage ring than the reference particle and a particle with less momentum than the reference particle ($\Delta p/p < 0$) needs less time. This is especially becoming important in the next section [15].

Synchrotron Frequency

Cavities are the parts of an accelerator in which a particle beam is accelerated, decelerated or bunched by electric fields. In a ring accelerator, it must be ensured that the circulating particles maintain a well-defined fixed phase ψ_s on average with respect to the high-frequency voltage U_0 of the cavity to achieve a focusing effect in the longitudinal phase space. This focusing effect is called phase focusing. The phase ψ_s is the critical parameter which decides how much energy the particle gains from running through the cavity. The energy balance of the reference particle for one turn is composed of the amount of energy the particle receives while passing through the cavity and the energy the particle loses during this turn in the storage ring W_0 , e.g. through synchrotron radiation [15]:

$$E_0 = eU_0 \sin \psi_s - W_0. \quad (3.27)$$

Any particle which is passing the cavity at a different phase $\psi_d = \psi_s + \Delta\psi$ receives an additional amount of energy ΔE . From comparing the amount of energy the reference particle receives from the cavity and the amount of energy an offset particle receives from the cavity a differential equation for the longitudinal motion can be derived which depends on the additional amount of energy an offset particle receives from the cavity ΔE , its the second derivation after time $\Delta\ddot{E}$ and the so called synchrotron frequency ω_s [15]:

$$\Delta\ddot{E} + \omega_s^2 \Delta E = 0 \quad (3.28)$$

$$\omega_s = \omega_0 \sqrt{-\frac{eU_0 h \cos \psi_s}{2\pi\beta^2 E} \left(\alpha_0 - \frac{1}{\gamma^2} \right)}. \quad (3.29)$$

Equation (3.28) is describing an harmonic oscillation with the frequency ω_s which is describing the oscillating of the offset particles around the reference particle in the longitudinal phase space. To achieve focusing in the longitudinal phase space equation (3.29) has to be a real quantity. The parameters ψ_s and γ determine if equation (3.29) is real or imaginary [15].

In case one is below transition energy $\gamma < \gamma_t$ one has to choose a phase $-(n \cdot \pi)/2 < \psi_s < +(n \cdot \pi)/2$ so that equation (3.29) is real. Here n denotes an arbitrary integer. If one insert theses phases in equation (3.27) and neglect the energy loss W_0 one can observe that the phases $-(n \cdot \pi)/2 < \psi_s < 0$ decelerate the reference particle and the phases $0 < \psi_s < +(n \cdot \pi)/2$ accelerate it. A phase of $\psi_s = 0$ is neither accelerating nor decelerating the reference particle [15].

The reason one uses the rising flank of the sinusoidal function for acceleration of the beam if one is below transition energy is that a particle with less momentum than the reference particle needs more time than the reference particle to arrive at the cavity. Therefore it arrives later than the reference particle at the cavity and receives an additional acceleration compared to the reference particle. A particle with more momentum than the reference particle arrives earlier at the cavity and receives less acceleration than the reference particle. This leads to the desired focusing effect in the longitudinal phase space and is sketched in figure (3.5) [15].

In case one is above transition energy $\gamma > \gamma_t$ one has to choose a phase $+(n \cdot \pi)/2 < \psi_s < +(3n \cdot \pi)/2$ so that equation (3.29) is real. Inserting theses phases again in equation (3.27) and neglect the energy loss W_0 one can observe that the phases $+(n \cdot \pi)/2 < \psi_s < +\pi$ accelerate the reference particle and the phases $+\pi < \psi_s < +(3n \cdot \pi)/2$ decelerate it. A phase of $\psi_s = \pi$ is neither accelerating nor decelerating the reference particle [15].

Therefore one uses the falling flank of the sinusoidal function for acceleration if one is above transition energy. As being above transition energy a particles with more momentum than the reference particle has to travel a longer distance and therefore arrives later at the cavity. Here it receives less energy than the reference particle. The reverse happens to particles with less momentum than the reference particle. This also leads to a focusing effect in the longitudinal phase space. A sketch of this is shown in figure (3.5) [15].

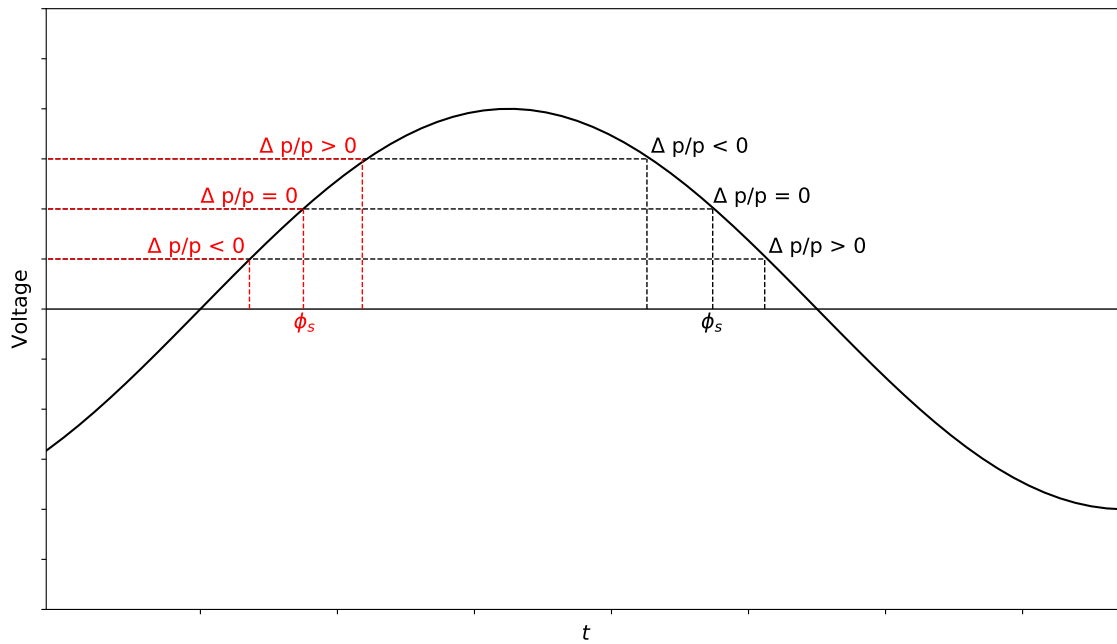


Figure 3.5: Principle of phase focusing. The x-axis shows the time at which the particle arrives at the cavity and the y-axis its voltage. The red lines represent the operation below transition and the black ones above transition. Inspired by [15].

3.3 Spin Dynamics

3.3.1 Spin Formalism

After explaining the particle motion in six-dimensional phase space, the motion of the spin must also be understood. The measurable quantity connected to the spin orientation of a particle ensemble is the polarization P . The polarization vector of a particle ensemble, which contains the expectation values of the spin operators is defined in the following way [17]:

$$\vec{P}_i = \frac{1}{N} \sum_{i=1}^N \vec{S}_i. \quad (3.30)$$

In case a beam consists of spin-1/2 particles two orientations of the spin with respect to the quantization axis are possible. These are $m = +1/2$ and $m = -1/2$. They define the vector polarization P_V along the quantization axis [17]:

$$P_V = \frac{N^{m=1/2} - N^{m=-1/2}}{N^{m=1/2} + N^{m=-1/2}}. \quad (3.31)$$

Considering instead spin-1 particles three orientations of the spin with respect to the quantization axis are possible which are $m = \pm 1$ and $m = 0$. In this case the vector polarization P_V and tensor polarization P_T along the quantization axis are [17]:

$$P_V = \frac{N^{m=1} - N^{m=-1}}{N^{m=1} + N^{m=0} + N^{m=-1}} \quad (3.32)$$

$$P_T = \frac{N^{m=1} + N^{m=-1} - 2N^{m=0}}{N^{m=1} + N^{m=0} + N^{m=-1}}. \quad (3.33)$$

3.3.2 Spin Motion

Spin motion and particle motion are closely linked. To describe this behavior, the evolution of the spin is determined by the electric \vec{E} and magnetic \vec{B} fields which a particle experiences inside the storage ring. The evolution of the spin in the center-of-mass system of the particle is:

$$\frac{d\vec{S}}{dt} = \vec{\mu} \times \vec{B} + \vec{d} \times \vec{E}. \quad (3.34)$$

Transforming the electromagnetic field in the laboratory system, in which it is usually known in a storage ring, leads to the Thomas-Bargmann-Michel-Telegdi (Thomas-BMT) equation [8]:

$$\frac{d\vec{S}}{dt} = \vec{\Omega} \times \vec{S} = \vec{\Omega}_{MDM} \times \vec{S} + \vec{\Omega}_{EDM} \times \vec{S}, \quad (3.35)$$

$$\vec{\Omega}_{MDM} = -\frac{q}{m} \left[\left(G + \frac{1}{\gamma} \right) \vec{B} - \frac{G\gamma}{\gamma+1} (\vec{\beta} \cdot \vec{B}) \vec{\beta} - \left(G + \frac{1}{\gamma+1} \right) \vec{\beta} \times \frac{\vec{E}}{c} \right], \quad (3.36)$$

$$\vec{\Omega}_{EDM} = -\frac{q}{mc} \frac{\eta_{EDM}}{2} \left[\vec{E} - \frac{\gamma}{\gamma+1} (\vec{\beta} \cdot \vec{E}) \vec{\beta} + c \vec{\beta} \times \vec{B} \right]. \quad (3.37)$$

In this equation the precession frequency $\vec{\Omega}_{MDM}$ shows the contribution of the MDM to the spin motion while $\vec{\Omega}_{EDM}$ shows the contribution of the EDM. The quantity G is the gyromagnetic anomaly $G = (g - 2)/2$ with the Lande's g factor. It is displayed for some particles in table (3.1).

Table 3.1: Magnetic properties of proton, electron and deuteron. The column 'Type' shows possible spin configurations and column ' $|\vec{\mu}'$ ' the MDM in units of Bohr's magneton μ_B . The quantity g shows Lande's g -factor and G the gyromagnetic anomaly [18].

Particle	Type	$ \vec{\mu}' $ in μ_B	g	G
Proton	$\pm 1/2$	2.792	5.585	+1.793
Electron	$\pm 1/2$	1.001	2.002	+0.001
Deuteron	$\pm 1, 0$	0.857	1.714	-0.142

In this table the second column shows to which polarization type the corresponding particle belongs. The third column shows Lande's g -factor which is closely connected to the gyromagnetic anomaly G in the fourth column.

As this thesis is focusing on the spin motion induced by the MDM its behavior has to be understood better. The precession due to the MDM can be divided into contributions of parallel \vec{B}_{\parallel} and perpendicular \vec{B}_{\perp} field components with respect to the velocity of the particles [9]:

$$\vec{\Omega}_{MDM} = -\frac{q}{\gamma m} \left[(1 + \gamma G) \vec{B}_{\perp} + (1 + G) \vec{B}_{\parallel} - \left(G\gamma + \frac{\gamma}{\gamma+1} \right) \vec{\beta} \times \frac{\vec{E}}{c} \right]. \quad (3.38)$$

As the spin motion and particle motion are coupled, the orientation of spin in relation to the particles momentum has to be considered. For this reason the cyclotron frequency Ω_{cyc} has to be taken into account. It describes the rotation of momentum induced by electromagnetic fields [9]:

$$\frac{d\vec{p}}{dt} = \vec{\Omega}_{cyc} \times \vec{p}, \quad (3.39)$$

$$\vec{\Omega}_{cyc} = -\frac{q}{\gamma m} \left(\vec{B}_{\perp} - \frac{1}{\beta^2} \vec{\beta} \times \frac{\vec{E}}{c} \right). \quad (3.40)$$

After subtracting equation (3.40) from equation (3.38) one receives a description of the spin precession relative to the momentum precession. The relative precession is defined as $\vec{\Omega}_{MDM,rel}$ [9]:

$$\vec{\Omega}_{MDM,rel} = -\frac{q}{\gamma m} \left[G\gamma \vec{B}_{\perp} + (1 + G)\vec{B}_{\parallel} - \left(G\gamma - \frac{\gamma}{\gamma^2 - 1} \right) \vec{\beta} \times \frac{\vec{E}}{c} \right]. \quad (3.41)$$

3.4 Principle of Electric Dipole Moment Measurement

In the following section a realistic case is considered where magnetic fields are vertically applied $\vec{B} = (0, B, 0)^T$ and electric fields are applied in radial direction $\vec{E} = (E, 0, 0)^T$. The particle itself is moving on the longitudinal axis with $\vec{\beta} = (0, 0, \beta)^T$. In result the MDM contribution to the spin precession is only able to rotate the spin vector in horizontal plane whereas the contribution to the precession due to EDM is able to rotate the spin vector in vertical plane. This behavior is illustrated in figure (3.6) [19].

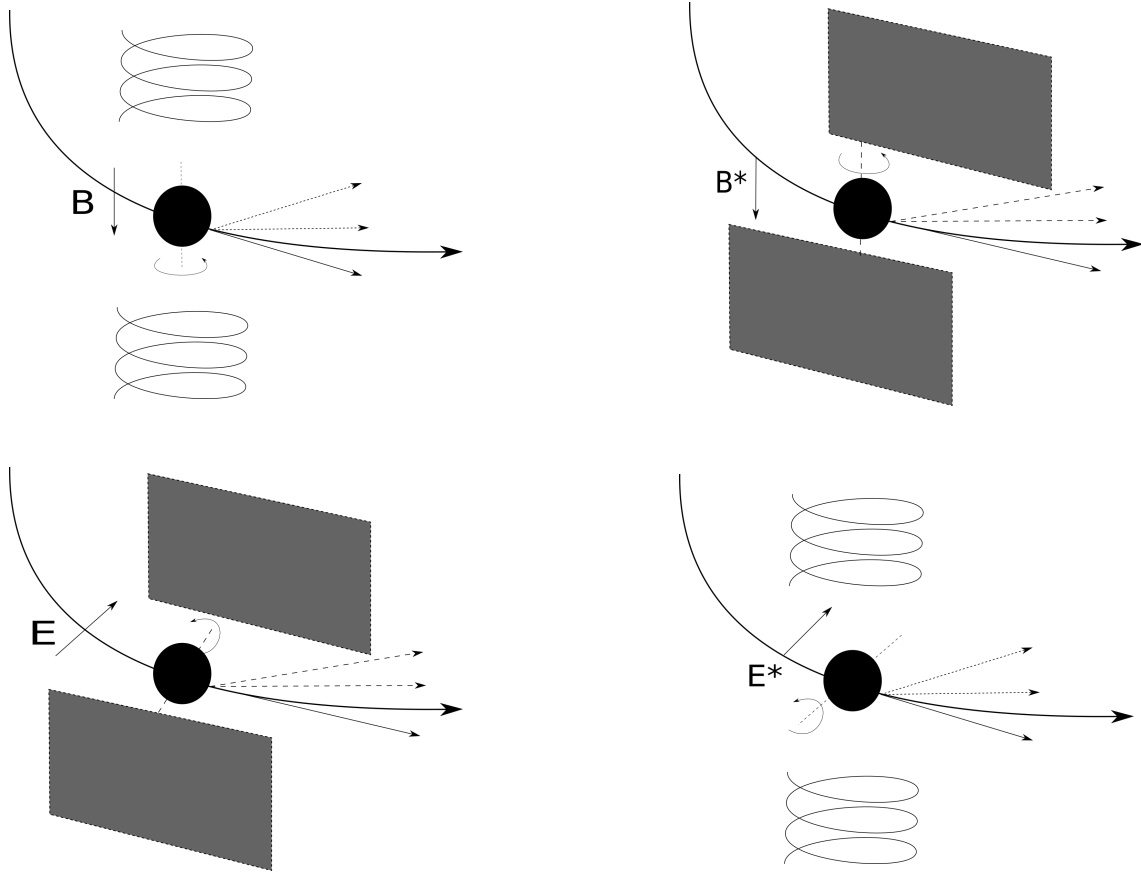


Figure 3.6: Sketch of spin rotation due to magnetic and electric fields. The upper images show the contribution of MDM to spin precession and the bottom ones the contribution of EDM. The cross product of \vec{B} and \vec{v} is marked with an E^* and the cross product of \vec{E} and \vec{v} with a B^* . Inspired by [19].

Through the horizontal rotation of the spin, electromagnetic fields cause the spin to rotate upwards in one revolution and downwards in another and vice versa. Thus, on average, no signal is obtained from the rotation due to EDM contribution. Only a direct signal from the vertical rotation due to EDM contribution can be detected if the horizontal rotation vanishes. This is called frozen spin.

The resulting polarization of a particle beam can be measured using a polarimeter which is recording the asymmetry in reaction rate. A spin which stays aligned to momentum is causing no asymmetry whereas a spin which is rotated in vertical direction is causing a left-right asymmetry in the polarimeter. A spin which is rotated in the horizontal is causing a up-down asymmetry [19].

3.4.1 Frozen Spin Method

As discussed previously the criterion for a direct measurement of the EDM is a vanishing horizontal rotation [19]:

$$\vec{\Omega}_{MDM} = -\frac{q}{\gamma m} \left[G\gamma B - \left(G\gamma - \frac{\gamma}{\gamma^2 - 1} \right) \beta E \right] \stackrel{!}{=} 0. \quad (3.42)$$

Pure Magnetic Storage Ring

A classic storage ring consists of magnetic elements but no electric elements. It is not possible to achieve any configuration in such a storage ring at which the criteria for frozen spin is fulfilled although it is mathematically possible. The reason for this is that a B field is needed to keep a particle inside the storage ring [19]:

$$G\gamma B \stackrel{!}{=} 0. \quad \zeta \quad (3.43)$$

Pure Electric Storage Ring

A purely electric storage ring is the exact opposite of a purely magnetic storage ring as only electric elements do have an impact of the particle and spin motion. In such a ring the criteria for frozen spin can be fulfilled via [19]:

$$\left(G\gamma - \frac{\gamma}{\gamma^2 - 1} \right) \beta E \stackrel{!}{=} 0, \quad (3.44)$$

$$\left(G\gamma - \frac{\gamma}{\gamma^2 - 1} \right) = 0 \quad \Rightarrow \quad p = \frac{mc}{\sqrt{G}}. \quad (3.45)$$

The corresponding momentum at which the spin is frozen is called magic momentum and is just depending on the particles properties. This also limits the number of particles where frozen spin can be achieved within a pure electric ring. Only particles with a positive G can have frozen spin in a pure electric storage ring but no particle with a negative G like deuterons [20].

Combined Fields

The spin can also be frozen in a storage ring with combined fields. The criteria which has to be fulfilled in this case is shown below [19]:

$$\Rightarrow B = \left(G - \frac{1}{\gamma^2 - 1} \right) \frac{\beta E}{G}. \quad (3.46)$$

From the fact that Lorentz force and centrifugal force have to be equal inside the bending elements to keep the particle inside the ring a second condition can be derived [21]:

$$q(\vec{E} + \vec{\beta} \times \vec{B}) = \frac{\gamma m \beta^2}{r}, \quad (3.47)$$

$$\Rightarrow E = \frac{\gamma m \beta^2}{qr} - \beta B. \quad (3.48)$$

Combing both conditions shown in the equations (3.46) and (3.48) a equation of determination for the fields strengths inside the bending elements can be derived [21]:

$$\Rightarrow E = \frac{\gamma m \beta^2}{qr} \frac{1}{\left(\frac{1}{\gamma^2 - 1} - G \right) \frac{\beta^2}{G} + 1}, \quad (3.49)$$

$$\Rightarrow B = \frac{\gamma m \beta^2}{qr} \frac{\left(\frac{1}{\gamma^2 - 1} - G \right) \frac{\beta}{G}}{\left(\frac{1}{\gamma^2 - 1} - G \right) \frac{\beta^2}{G} + 1}. \quad (3.50)$$

It can be seen that in the case of combined fields, it no longer matters whether particles with positive or negative G were used. As long as the required field sizes can be achieved in any accelerator with combined bending elements frozen spin can be used [20].

3.4.2 Spin Tune Spread and Spin Coherence Time

The spin tune spread and the SCT are the critical parameter when performing EDM experiments in storage rings. They are defined for a particle bunch und show how fast initially aligned spins diverge due to the different fields the individual particles see. To understand both quantities the spins of the individual particles must be transformed into a polarization which is shown in equation (3.30). In a second step the Cartesian spin polarization has to be transformed in a spherical spin polarization. Figure (3.7) and the following equations are explaining the transformation rules:

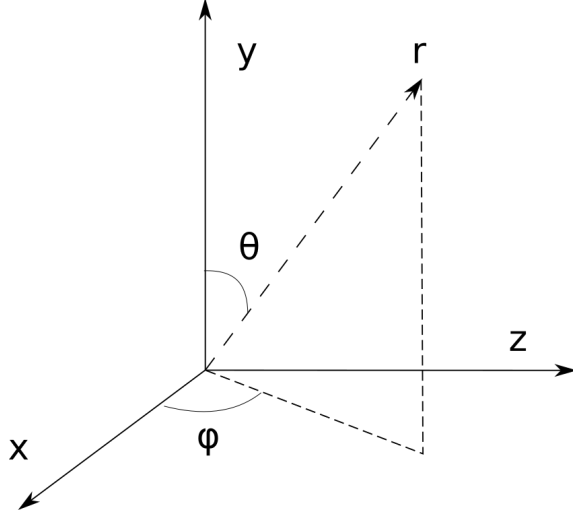


Figure 3.7: Transformation from Cartesian coordinate system to spherical coordinate system for the spin polarization formalism where x , y and z are the Cartesian coordinates. The quantity r shows the radial distance, ϕ the polar angle and θ the azimuthal angle.

$$P_{tot} = \sqrt{P_x^2 + P_y^2 + P_z^2} \quad (3.51)$$

$$\phi_{P,beam} = \tan^{-1}(P_x/P_z) \quad (3.52)$$

$$\theta_{P,beam} = \cos^{-1}(P_y/P_{tot}). \quad (3.53)$$

The SCT is defined as the time at which the total spin polarization P_{tot} is falling below $1/e$. Therefore describes how fast the beam is losing its polarization and becomes decoherent. Another important property is $\phi_{P,beam}$ which directly connected to the spin tune spread $\Delta\nu_s$. The spin tune spread describes the amount of horizontal rotation of the polarization in one turn relative to the reference particle's spin rotation ν_s which is called spin tune [9]:

$$\Delta\nu_s = \frac{\sum_i (\phi_{P,beam}^i - \nu_s)}{\sum_i 2\pi}. \quad (3.54)$$

3.4.3 Depolarizing Spin Resonances

Similar to the resonances due to the betatron oscillations one has to consider spin resonances which are able to reduce the SCT. They occur around areas where the spin tune ν_s of the reference particle fulfills a resonance condition. Spin resonances of different type are summarized in table (3.2) [9].

Table 3.2: Summary of depolarizing spin resonances. The property ν_s shows the spin tune of the reference particle and the k, l, m and n are integer. Horizontal and vertical betatron tune are represented via Q_x and Q_y and the longitudinal tune with Q_s . The quantity P shows the super periodicity of the storage ring design [9].

Type	Case	Origin
Imperfection resonance	$\nu_s = k$	Field and positioning errors of magnets
Intrinsic resonance	$\nu_s = kP \pm Q_y$	Horizontal fields for vertical focusing
Higher-order resonance	$\nu_s = (k \pm l \cdot Q_x \pm m \cdot Q_y \pm n \cdot Q_s)$	Higher-order field errors of magnets and synchrotron motion

4 Prototype EDM Storage Ring

4.1 Project Overview

The Jülich Electric Dipole moment Investigations (JEDI) collaboration was created in the end of 2011. The group is aiming to carry out a long term project for the measurement of the permanent EDM of a proton and deuteron in a storage ring. In order to develop the final high precision experiment, a strategy is proposed that consists of three stages. The special features of each stage are summarized in table (4.1) [22].

The aim of the first stage of the strategy is the demonstration of the feasibility of critical technologies for EDM measurement. Therefore the already existing facility is used. The COSY is a pure magnetic storage ring where polarized deuteron beams can be investigated. Since the spin of the deuterons is non-frozen, the polarization rotates in the horizontal plane. A so called RF Wien Filter that oscillates at the polarization precession frequency and has its magnetic axis vertically aligned is used to recover an EDM signal [23].

For the second step a new facility the so called prototype EDM storage ring has to be constructed. The reason to build this facility is the demonstration of frozen spin inside a storage ring. Also spin manipulation tools should be developed with the new facility and an increased-precision EDM value should be measured. The frozen spin condition in this relatively small storage ring can be achieved by using a combination of magnetic and electric fields inside the bending devices. Another feature which should be established with the prototype EDM ring is the injection and operation of two counter circulating beams at the same time. This method can eliminate a large fraction of systematic errors by looking at the difference between the two counter circulating beams [23].

The final stage of strategy is the construction and operation of a pure electric storage ring where no magnetic field is influencing the proton spin. This ring will be a larger version of the prototype ring which does have the same features of frozen spin and counter circulating beams. This ring will need all the technology developed in the previous stages and allows for a high precision measurement of the proton EDM signal [23].

Table 4.1: Summary of important features of proposed stages in the EDM research strategy.

Cooler Synchrotron	Prototype Storage Ring	All Electric Ring
Proof-of-Capability	Proof-of-Principle	Precession Experiment
Pure Magnetic	Electric and Magnetic	Pure Electric
Deuterons	Protons	Protons, Deuterons, ^3He
Non-Frozen Spin	Frozen Spin	Frozen Spin
Single Beam	Counter-circulating Beams	Counter-circulating Beams

This thesis is focusing on the simulation of some properties of the prototype EDM storage ring. In the following section the current design and its integration into the simulation software Bmad will be discussed.

4.2 Design

The current design of the prototype EDM ring is based on a version made in February 2020 and consists of four unit cells. In between each unit one quadrupole is placed to add additional tuning possibilities. Each unit cell has the following structure which provides a total bending of 90° [3]:

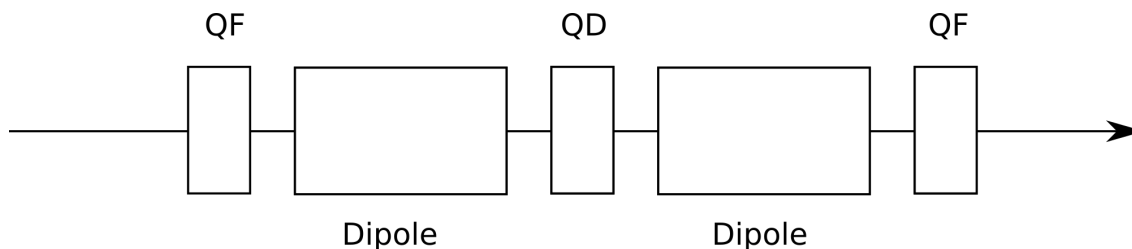


Figure 4.1: Layout of a unit cell. 'QD' belongs to the horizontally defocusing quadrupole family and 'QF' to the horizontally focusing quadrupole family.

Summing up all the magnets placed in the basic form of the lattice one ends up with eight dipoles and 16 quadrupoles. The quadrupoles can be structured into three families with common power supplies. In the bending section, i.e. in between the bending dipoles of one unit cell the quadrupoles of the first family were placed. This family was named 'QD' and contains four quadrupoles in total. The quadrupoles around the bending dipoles of one unit cell form the next family which is called 'QF' which contains over all eight quadrupoles. The last family consist of those quadrupoles which were placed in between the unit cells. These are called 'QSS' as they are placed in the straight sections of the storage ring. This family contains four quadrupoles and provides further flexibility to adjust the beam optics [3].

In a very simple approach a sextupole was placed on top of every quadrupole to correct chromaticity right at the place of origin. Also these sextupoles form three families which correspond to the quadrupole families. They are named similar to the associated quadrupole families they belong to with 'SXF', 'SXD' and 'SXSS'. A sketch of the design with clockwise (CW) and counter-clockwise (CCW) injection is shown in figure (4.2) and all the elements used are summarized in table (4.2). The kinematic parameters of the reference particle are shown in table (4.3) [3].

Table 4.2: Summary of lattice elements.

Element	Number	Length
Dipole	8	9.61975 m
Quadrupole	16	0.40000 m
Sextupole	16	0.40000 m
Cavity	1	1.00000 m

Table 4.3: Kinematic parameters of reference particle.

Parameter	Magnitude	Unit
Kinetic Energy	0.045	GeV
Momentum	0.294	GeV
β	0.299	/
γ	1.048	/

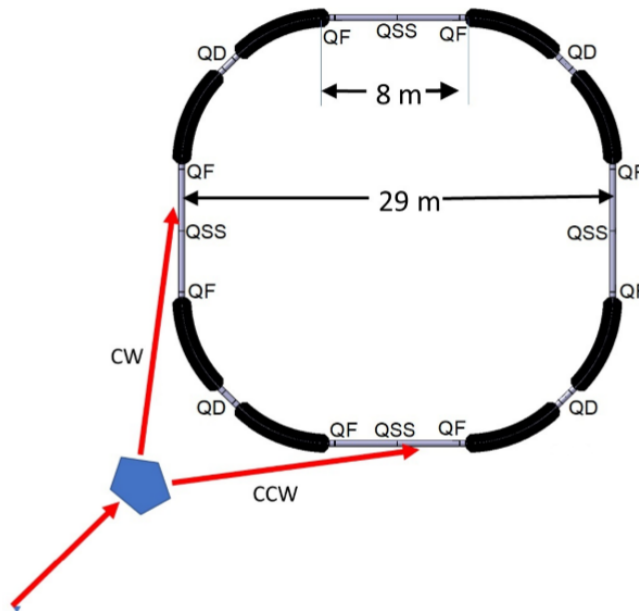


Figure 4.2: Basic layout of the prototype EDM storage ring. Injection lines for CW and CCW injecting indicated as red arrows. QD is the horizontal focusing quadrupole family, QF the horizontal defocusing quadrupole family and QSS a quadrupole family which provides further flexibility to adjust the beam optics. The total circumference of the ring is approximately 123 m. Version 2018 [3].

The strength of the magnetic and electric field of the dipoles just depend on the particle's momentum and the length of dipoles as demonstrated in equation (3.49) and (3.50). For the previously presented design, the magnetic and electric field strengths read:

$$|E_{\text{dipole}}| = 5.061 \text{ kV/m} \quad (4.1)$$

$$|B_{\text{dipole}}| = 0.024 \text{ T}. \quad (4.2)$$

As the unit cells and the length of each element is now defined the circumference and the width of the design just depend on the length of the straight sections in between the bending sections. In the design version of the prototype ring of February 2020 one is facing a total circumference of $C = 123.358 \text{ m}$ and a width from beam line to beam line of 36.252 m . The length of the straights in the current version is 12.648 m . With these parameters the revolution frequency ν and the time for one revolution τ for the design particle is given by:

$$\nu = \frac{pc}{C\sqrt{p^2 + m^2}} = 726.794 \text{ kHz} \quad (4.3)$$

$$\Rightarrow \tau = \frac{1}{\nu} = 1.375 \text{ } \mu\text{s}. \quad (4.4)$$

4.3 Implementation into Bmad

The simulation of this design of the prototype EDM ring has been performed with Bmad which is a subroutine library for charged-particle tracking in storage rings. It has been developed at Cornell University's Laboratory for Elementary Particle Physics. The subroutine library is using an object oriented approach and is written in Fortran. Bmad can be used to study single as well as multi-particle beam dynamics. For this reason it has various tracking algorithms including the Runge-Kutta and symplectic integration. It also provides routines for calculating transfer matrices, emittances, Twiss parameters, and dispersion. Some elements which are already included in Bmad are dipoles, quadrupoles, sextupoles and RF cavities which is everything one needs to simulate the basic version of the prototype ring [24].

Although all necessary elements are already defined in Bmad the construction of dipoles which make use of combined magnetic and electric fields is challenging. The solution is the correct manipulation of parameters of a magnetic dipole magnet. For this purpose a

4.4 Benchmarking the Model

4.4.1 Definition of Phase Space

In order to benchmark the model one first has to define the phase space coordinates of the particle in the six dimensional phase space in Bmad. The horizontal X and vertical Y phase space coordinates describe the physical offset of a particle from the design orbit. Their corresponding momenta P_x and P_y display the momenta in horizontal p_x and vertical p_y direction normalized by the design particle momentum p_0 [24]:

$$P_x(s) = \frac{p_x(s)}{p_0} \quad (4.5)$$

$$P_y(s) = \frac{p_y(s)}{p_0}. \quad (4.6)$$

Dealing with the longitudinal phase space is more complicated as the longitudinal phase space coordinate Z should not be confounded with the longitudinal offset of a particle from the design orbit. The phase space coordinate Z is defined by the difference in time it needs to reach the same point as the reference particle [24]:

$$Z(s) = \beta(s) \cdot c \cdot (t(s) - t_0(s)) \quad (4.7)$$

The phase space which corresponds to the longitudinal momentum contains the information of the overall particle momentum as it is defined by the difference of the design momentum and also normalized by it [24]:

$$P_z(s) = \frac{p(s) - p_0}{p_0}. \quad (4.8)$$

In the following chapters and sections these definitions of the six dimensional phase space will be used.

4.4.2 Investigation of numerical noise

Knowing how Bmad treats the phase space coordinate one is able to investigate the closed orbit of the model of the prototype EDM storage ring. An arbitrary working point has been chosen for this reason. A discussion which working points allow stable operation will be performed later. Bmad is able to calculate the closed orbit of a lattice using the subroutine *closed_orbit_calc*. The results of this subroutine are shown in figure (4.4).

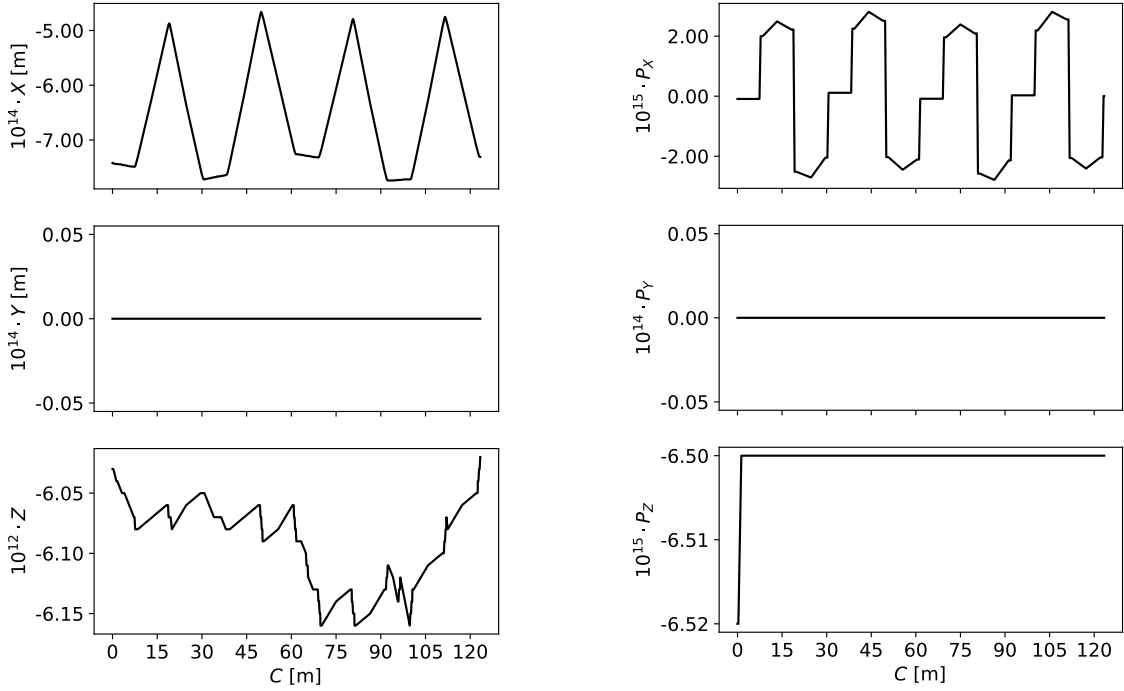


Figure 4.4: Closed orbit and momentum deviation for a randomly selected working point of the storage ring. While the x-axis indicates the position in the memory ring for all plots, the y-axis changes for each plot. The y-axes of the two upper plots show the horizontal phase space, where the physical offset X to the reference particle is shown on the left and the momentum deviation P_X on the right. The same is shown by the two middle plots for the vertical phase space and by the two bottom plots for the longitudinal phase space.

In this figure one can see how the phase space coordinates of the closed orbit are changing over the ring circumference. The upper plots show the horizontal phase space, whereas the lower ones show the vertical phase space. The bottom plots contain the information about the longitudinal phase space. On the x-axis one can see the position s in the rings circumference.

The plots for the horizontal phase space and the longitudinal phase space show some numerical noise which may come from round off errors due to the dipoles. This assumption is supported by the fact that there is a fourfold periodic structure visible in the horizontal phase space. The beginning and end of each periodic structure in the horizontal phase space is in good agreement with the beginning and the end of the unit cell of the model. The vertical phase space does not show any numerical noise which is not surprising as the vertical phase space is not influenced by the dipoles.

In order to check if the numerical noise has an impact on a particle which is starting on the closed orbit and has the properties of the design particle, a particle with these features was tracked over 10000 turns. For this investigation the Bmad subroutine *track_all* was used which as the name suggests is tracking a particle through the lattice. The results are shown in figure (4.5).

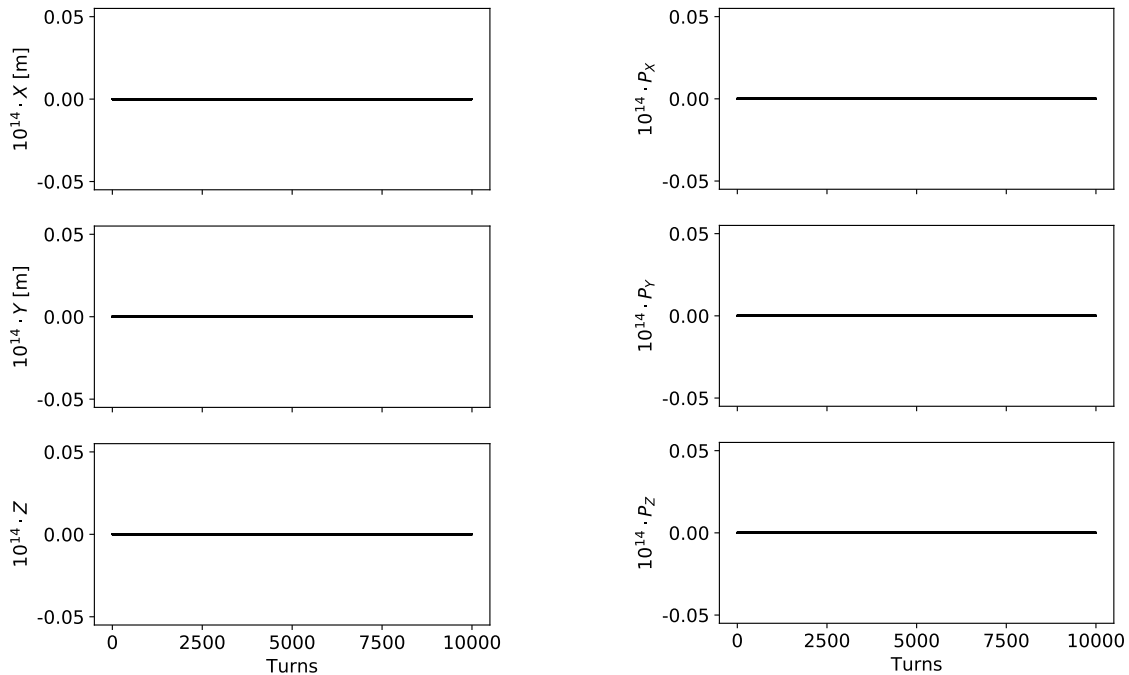


Figure 4.5: Evolution of phase space over 10000 turns for a particle which is starting on the closed orbit and has the properties of the design particle. While the x-axis indicates the number of tracked turns for all plots, the y-axis changes for each plot. The y-axes of the two upper plots show the horizontal phase space, where the physical offset X to the reference particle is shown on the left and the momentum deviation P_X on the right. The same is shown by the two middle plots for the vertical phase space and by the two bottom plots for the longitudinal phase space.

This figure has the same structure as the one before. It is showing the horizontal phase space in the upper plots, the vertical phase space in the plots below and the longitudinal phase space in the bottom plots. In contrast to the previous figure the x-axis shows the turn number at which the phase space was determined. The phase space was always recorded at the beginning element of the lattice.

This investigation shows that the numerical noise does not influence the tracked particle at all. For this reason one is able to call this particle the reference particle. Similar plots can be shown for any working point which allows stable operation.

4.4.3 Dipole fields and frozen spin

One now has to check if the spin is actually frozen for the design particle. Therefore the electric and magnetic fields of the bending dipoles have been investigated. A routine was written which tracks a particle on the reference orbit through a dipole and records the electric and magnetic fields it experiences. The results of this routine are shown in figure (4.6).

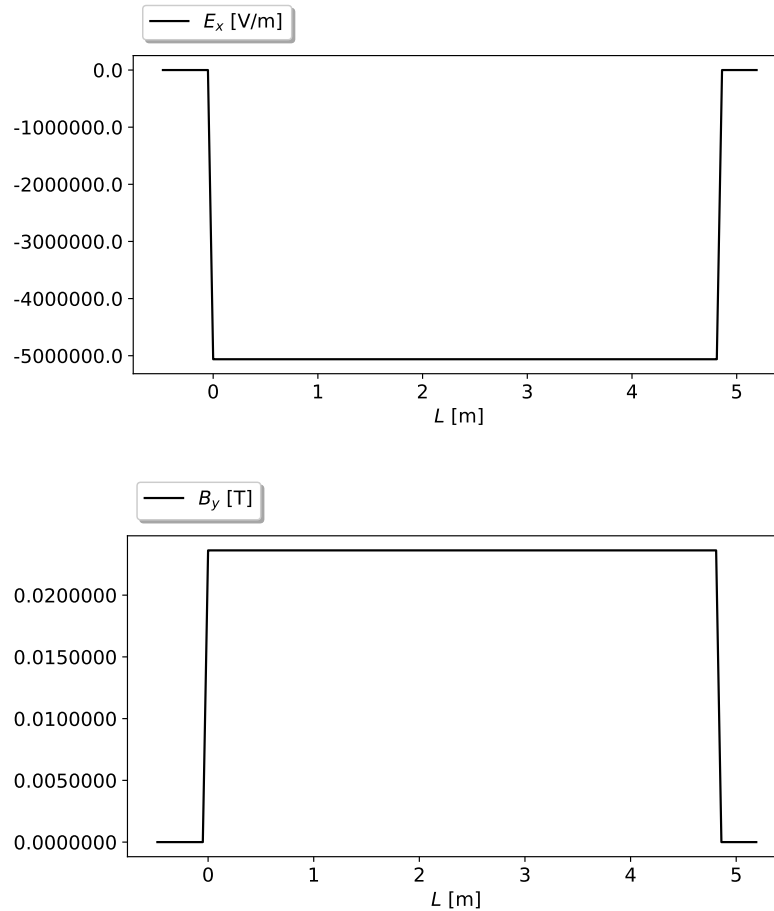


Figure 4.6: Electric and magnetic field inside the dipoles. The x-axis shows the position inside the dipole while the y-axis shows the field strength.

In this figure the upper plot shows the horizontal electric field component and the lower one shows the vertical magnetic field component. The x-axis shows the longitudinal position inside the dipole. Only these field components were present inside the dipoles. All other field components show zero strength. The magnitude of the visible fields are in perfect agreement with the fields which are shown in equation (4.1) and equation (4.2). Another observation which is important is that the fields arise immediately and with full strength after the particle enters the dipole. When the particle leaves the dipole the fields vanish instantaneously. This shows that the desired box fields are achieved and one considers dipoles without fringe fields.

With these fields the reference particle spin has to be frozen. To check if this is the case the reference particle spin was tracked for 10000 turns with spin and momentum initially aligned. The Cartesian and the spherical spin vectors coordinates have been investigated. The transformation from Cartesian spin coordinates to spherical spin coordinates is identical to the one sketched by figure (3.7) and shown in the equations (3.51),(3.52) and (3.53).

The results of the investigation of the spin vectors are shown in figure (4.7). It shows the Cartesian spin vectors on the left side and the spherical spin vectors on the right side. The Cartesian coordinate system and the spherical coordinate system are defined alongside the co-moving coordinate system. The important observation in these plots is that the spin is not rotating if the reference particle is tracked. All plots show constant values over 10000 turns. The presented benchmarking simulations prove that all important features of the prototype EDM ring were successfully implemented into the Bmad model.

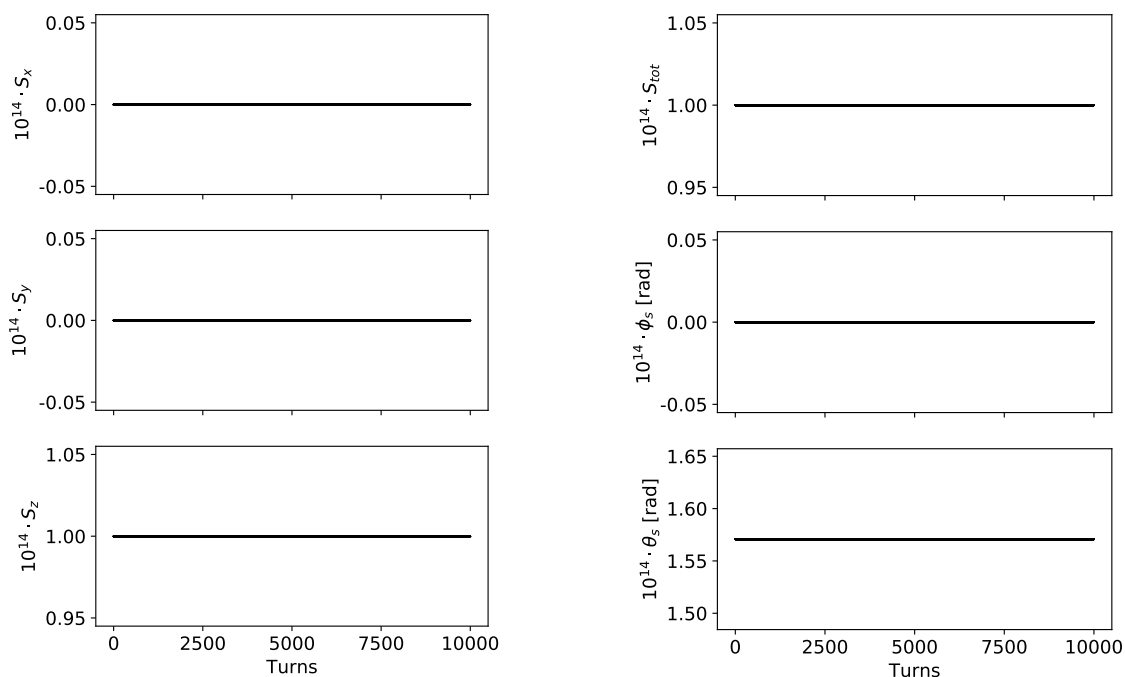


Figure 4.7: Evolution of spin coordinates over 10000 turns for a particle which is starting on the closed orbit and has spin and momentum initially aligned. While the x-axis indicates the number of tracked turns for all plots, the y-axis changes for each plot. On the left side the y-axis shows the Cartesian spin coordinates. On top the horizontal spin coordinate S_x is shown, below the vertical spin coordinate S_y and at the bottom the longitudinal spin coordinate S_z . On the right side the y-axis shows the spherical spin coordinates. On top the total spin S_{tot} is shown, below polar angular ϕ_s and at the bottom the azimuthal angular θ_s .

4.4.4 Phase Space Ellipse

In order to study realistic situations, the behavior of particles with an offset in phase space has to be investigated. A first important observation was that particles which had a spacial or a momentum offset beyond a specific limit were lost during tracking. As also the dynamic aperture is limited this is reasonable. For particles which have a spacial or a momentum offset which is inside this limit it is important to check if the six dimensional phase space is conserved. This was done by recording the phase space ellipse at the beginning of the lattice and at an arbitrary point inside the lattice over 10000 turns. Figure (4.8) shows the results.

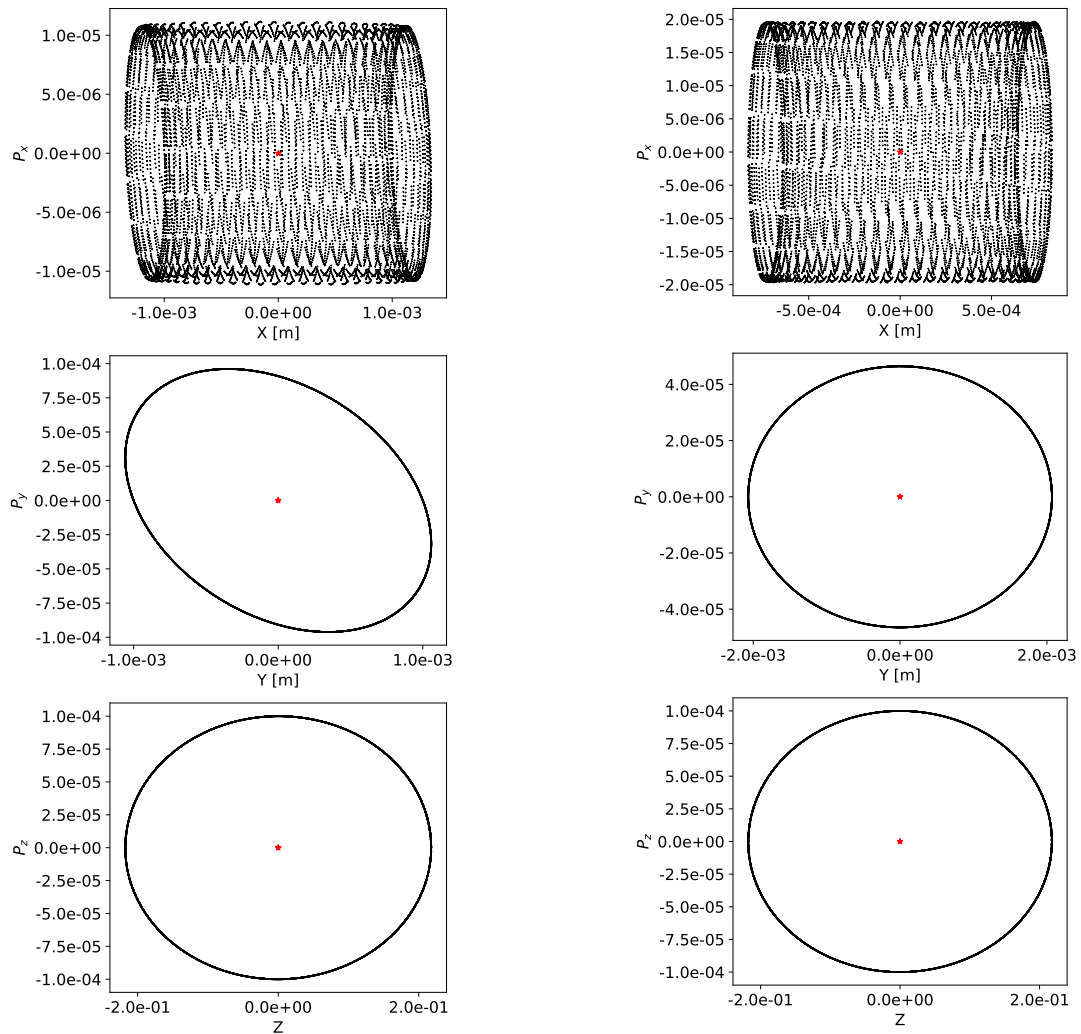


Figure 4.8: Phase space ellipses at two different locations for a particle with offsets in all phase space coordinates. One location is shown on the left side and the other on the right side. The upper plots show horizontal phase space ellipses, the ones below vertical phase space ellipses and the bottom ones longitudinal phase space ellipses. The center of the ellipses estimated by an elliptic fit is marked with a red dot.

The plots on the left side of the figure show the phase space ellipses at the beginning of the lattice and the plots on the right side of the figure show the phase space ellipses at an arbitrary point inside the lattice. The y-axis is always showing the phase space momentum and the x-axis the corresponding phase space vector. Each black dot inside these graphs represents the result of one turn around the storage ring. The red dot inside these graphs mark the center of the ellipses which was determined using an elliptic fit.

The phase space ellipses for the vertical and the longitudinal phase space fulfill the expectation as the corresponding graphs at both locations inside the ring show ellipses. This can be observed at any location. The areas of these ellipses are identical which shows that the phase space is conserved. The ellipses are centered around the origin of the plots. The origin represents the reference particles location as it was shown before.

Understanding the graph for the horizontal phase is more complicated. They show a cylindrical structure and not a simple ellipse as in the other plots. The reason for this is that an offset particle is moving on dispersive trajectories. Due to the cavity, the center of the phase space ellipse is shifted on the x-axis. The limits of the shifted center are defined by the initial offsets of the particle. In the case of the horizontal phase space ellipse in figure (4.8) an initial spatial offset of 10^{-3} was chosen for the horizontal phase space. In result the center of the ellipse is moving in between $\pm 10^{-3}$. This movement of the center forms the symmetric cylindrical structure we are facing here. The area of this movement is identical at each point inside the accelerator. This shows that also the horizontal phase space is conserved.

As the model of the prototype EDM storage ring is benchmarked with these observations one is able to start further investigations.

5 Optical Flexibility of the Lattice

5.1 The Working Point

Possible working points for the lattice had to be investigated to choose an appropriate one for beam and spin tracking. Changing from one working point to another is done by varying quadrupole strengths. For this reason a scanning routine was written which worked in the following way:

1. All quadrupoles of family 'QF' were assumed to operate at the same strength. The same assumption was taken for all quadrupoles of family 'QD'. The quadrupole family 'QSS' was turned off and not considered in this routine.
2. While the strength of family 'QD' was kept constant, the strength of family 'QF' was modified. The fineness of the scan could be changed by the amount of variation chosen. After family 'QF' reached a predefined final strength it was set back to its initial strength.
3. After one iteration of the previous step the strength of family 'QD' was varied while the strength of family 'QF' was kept constant. The same step size as the one used for family 'QF' was applied to increase the strength of family 'QD' once. After this is done the previous procedure is performed again.
4. The two procedures were repeated until family 'QD' was varied between the same initial quadrupole strength and final quadrupole strengths as family 'QF'. After every variation of strength the horizontal and vertical tunes were calculated.

This routine allows a scan of the tune flexibility when using the quadrupole families 'QF' and 'QD'. The results of this routine for the current lattice are shown in figure (5.1) and (5.2). The step size chosen was $n = 10^{-2}$ and both families were varied in between normalized quadrupole field strengths of $k = \pm 0.4$ [1/m].

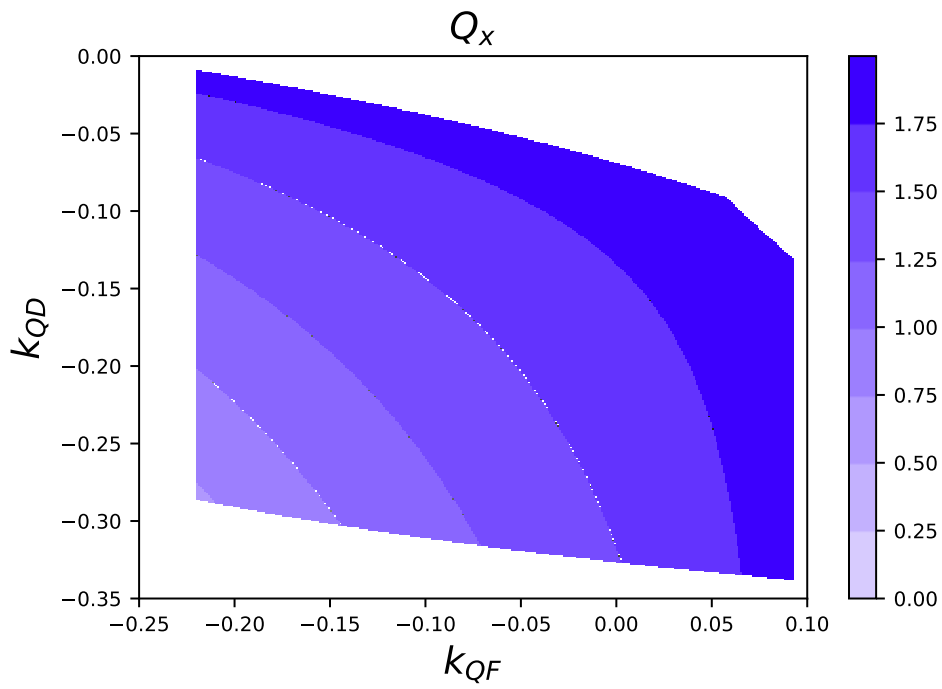


Figure 5.1: Horizontal betatron tune during the variation of the normalized quadrupole field strength k of the 'QF' and 'QD' quadrupole family. The colorbar indicates the magnitude of the horizontal tune.

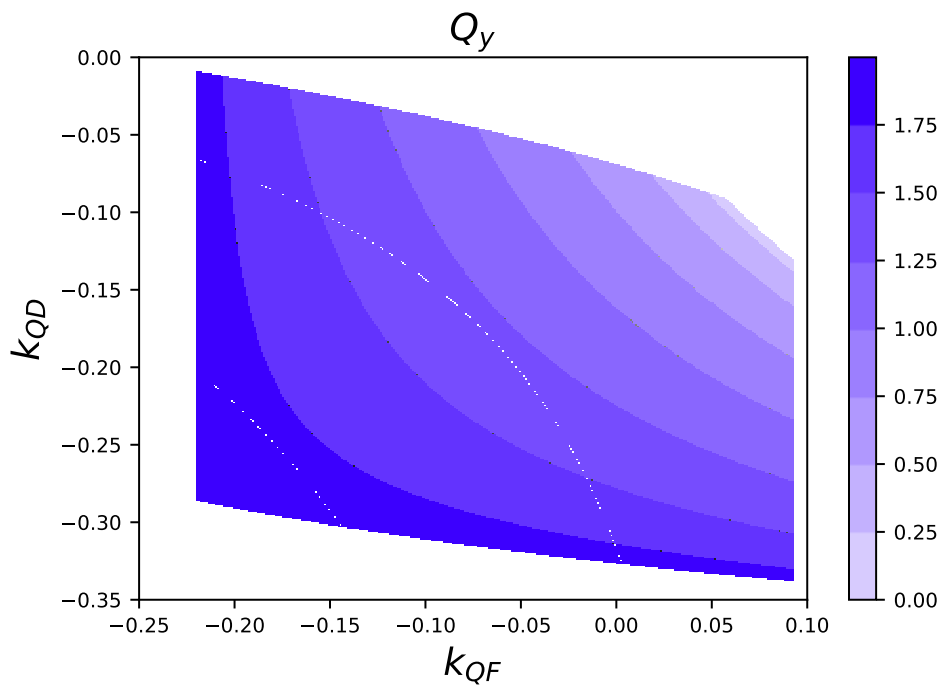


Figure 5.2: Vertical betatron tune during the variation of the normalized quadrupole field strength k of the 'QF' and 'QD' quadrupole family. The colorbar indicates the magnitude of the vertical tune.

Figure (5.1) and figure (5.2) display the strength of family 'QF' on the x-axis and the strength of family 'QD' on the y-axis. If no stable solution was found for the configuration of quadrupole strength a white dot is plotted. In case a stable solution was found the plotted dot is blue. Depending on the magnitude of the tune the dot is lighter or darker colored. The color bar on the right side of the figures gives more information about the magnitude of horizontal and the vertical tune.

As the quadrupole strength was varied in between values of $k = \pm 0.4$ [1/m] for both groups one might wonder why this is not shown in the figures. This is because only a limited amount of quadrupoles configurations allow stable operation. This limited amount of configurations is shown in the figures where these configurations form an area of stable operation. The values of $k = \pm 0.4$ [1/m] are not arbitrarily chosen. These were expected values in the case of pure electric quadrupoles [26].

Inside the area of stable operation the horizontal and vertical tunes are able to vary in between zero and two. The horizontal tune is increasing from low tune values in the lower left side of the area of stable operation to tune values close to two in the upper right side of the area of stable operation. The vertical tune is behaving vice versa and has very low tune values on the upper right side of the area of stable operation and tune values close to zero at the lower left side of the area of stable operation.

One can conclude that the area of stable operation is limited by the fact that either the vertical or horizontal tune hits a value of zero or two which is a first order betatron resonance. Beyond these tune values no further stable operation is possible. This is causing the sharp edges of the colored area. Also white lines inside the area of stable operation are visible which indicate working points of unstable operation. These white lines are at points where the horizontal tune fulfills a resonance condition. One might wonder why no white lines which correspond to resonance conditions induced by the vertical tune are visible. An explanation for this is provided by the fact that the chosen step size $n = 10^{-2}$ was not fine enough to reveal these unstable working points. They become visible at a much finer step size of $n = 10^{-7}$. In this idealized case no non-linear fields are implemented. For this reason no higher order resonances are visible. This is not the case in a real storage ring where the area of stable operation is even more limited.

As one now knows the tunes of the working points which allow stable operation one has to investigate the chromaticity at these working points to choose an appropriate working point for beam and spin tracking .

5.2 The Chromaticity

Chromaticity is a critical parameter in a storage ring. It describes the change in betatron tune with the relative momentum deviation and is described with formula (3.20). Therefore it is very important to know and understand the chromaticity at a chosen working point. To investigate the chromaticity the previous described scanning routine was used which varied the quadrupole strengths. In parallel another routine to access the chromaticity was implemented. It was inserted at the point in which the tunes were calculated in the scanning routine and worked in the following way:

1. The cavity and all sextupoles in the lattice were turned off.
2. Two particles were defined and placed on the closed orbit of the reference particle. One of this two particles receives an arbitrary positive momentum offset and the other one a corresponding negative momentum offset. It should be taken care that the momentum offsets are reasonable small so the particle performs a stable motion.
3. The closed orbits for the two offset particles are calculated. Based on the closed orbits the horizontal and the vertical betatron tunes are determined.
4. By comparing the tunes of the particle with the positive momentum offset and the particle with the negative momentum offset the chromaticity can be calculated according to:

$$\xi_i = \frac{Q_{i,+} - Q_{i,-}}{2 \cdot p_{\text{offset}}}. \quad (5.1)$$

This procedure is already included into the Bmad source code and called *chrom_calc*. To investigate the chromaticity of the prototype EDM storage ring a momentum offset of $p_{\text{offset}} = 10^{-4}$ was used in this routine. The results of this research are shown in the figure (5.3) and figure (5.4). The basic structure of figure (5.3) and figure (5.4) is identical to the structure of (5.1) and figure (5.2). The difference is lying in the color of dots which indicate stable operation. If the chromaticity at a working point with stable operation is negative this is marked with a red dot. In case the chromaticity is positive instead it is marked with a blue dot. The magnitude of the chromaticity is displayed with darker and lighter colors. The more the chromaticity deviates from zero the darker the color becomes. In case the chromaticity exceeds an absolute value of four it is kept at a value of four.

The results show that the chromaticity can vary widely when changing the quadrupole strengths and is also able to change sign. This results can not be understood when just considering quadrupole contributions to the chromaticity as it is done for large machines with strong focusing.

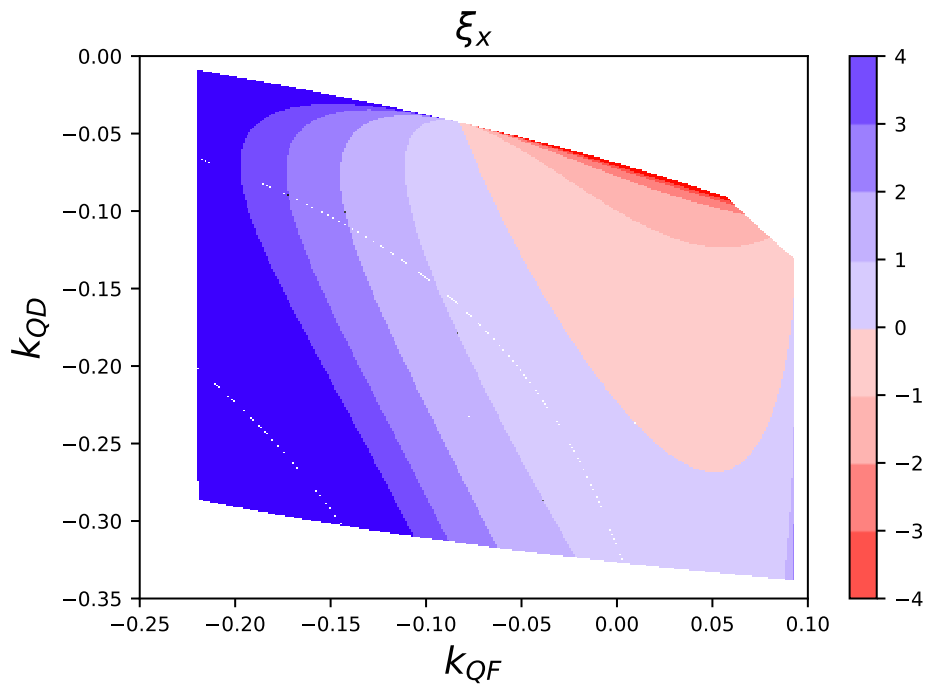


Figure 5.3: Horizontal chromaticity during the variation of the normalized quadrupole field strength k of the 'QF' and 'QD' quadrupole family. The colorbar indicates the magnitude of the chromaticity.

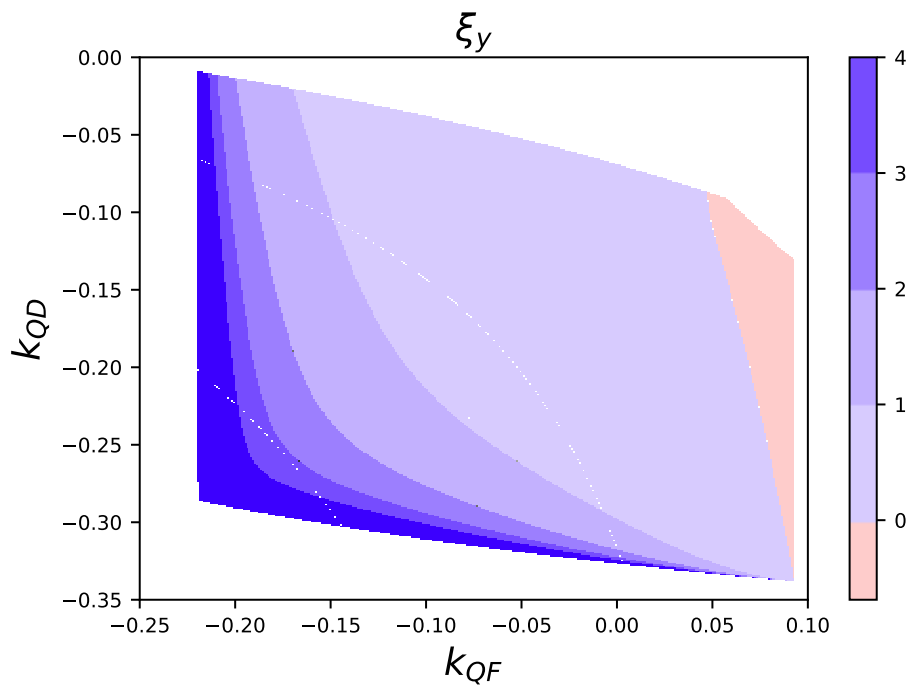


Figure 5.4: Vertical chromaticity during the variation of the normalized quadrupole field strength k of the 'QF' and 'QD' quadrupole family. The colorbar indicates the magnitude of the chromaticity.

5.2.1 Discussion of chromaticity for small rings

The chromaticity of large storage rings with strong focusing is dominated by the contribution of quadrupoles and sextupoles. When the ring is shrinking which means the bending radii become small this approach is susceptible to errors. Other contributions to the chromaticity become important as well. This is discussed in [27]. In the following this paper is summarized and the results for chromaticity are considered in relation to it:

Chromaticity arises from all momentum depend elements inside a storage ring. These are in particular dipoles, quadrupoles and sextupoles in the case of the prototype EDM ring. Also the location, size and shape of the closed orbit is momentum dependent and therefore influences the chromaticity. All effects caused by momentum dependent elements and the closed orbit have to be included into analytical models to give a correct prediction of chromaticities.

Especially important for rings with small bending radii are non-linear dipole contributions to the chromaticity which produce sextupole like effects. This can be understood considering the Hamiltonian of a dipole:

$$H_{\text{dipole}} = -[C/(2\pi\rho_0)] \times [Q_p[(1 + \delta)^2 - P_p^2 - P_z^2] - (C/\rho_0)(1/2)Q_p^2]. \quad (5.2)$$

Expanding the Hamiltonian by a power series around the design orbit it will contain linear, quadratic, cubic and higher order terms. The cubic terms are of the following form:

$$H_{\text{dipole}}^{\text{cubic}} \propto (C/\rho_0)(Q_p - Q_p^0)(P_p^2 + P_z^2)/(1 + \delta). \quad (5.3)$$

The term $(Q_p - Q_p^0)$ corresponds to the horizontal displacement from the design orbit divided by the circumference and therefore scales with the size of the ring. All other parameters are independent from the size of the ring. This cubic term has a large contribution to the chromaticity when considering small rings. For this reason chromaticity calculations that do not consider dipoles or just consider them to contribute linearly to the chromaticity are not expected to be correct for small rings.

A chromaticity calculation which is considering this non-linear dipole contribution and therefore can be used as a benchmark is the one Bmad is using inside the routine *chrom_calc* and which is explained at the beginning of this chapter. This also in agreement with the method the paper is recommending to calculate the chromaticity for small rings.

5.2.2 Discussion of chromaticity for large rings

To sketch the influence of non linear dipole contributions for this thesis an investigation was performed which compared the prediction of equation (3.21) for the natural chromaticity with the results of Bmad. Both lattices used for the following simulations consist of a repetitive sequence of dipoles and quadrupoles which form one unit cell as it is shown here:

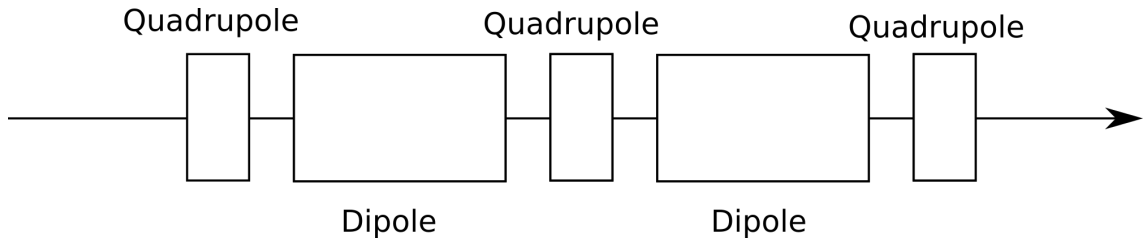


Figure 5.5: Layout of a unit cell.

This unit cell was used eight times to create a small lattice with a circumference of 68 m. In addition a larger lattice was designed by 32 of these unit cells which had a circumference of 272 m. To face a closed geometry only the bending radii of the pure magnetic dipoles had to be manipulated. All other parameter were kept constant. For this reason the bending radii of the larger ring are four times larger than the ones used in the small ring. A floor plan of both lattices is shown in figure (5.6).

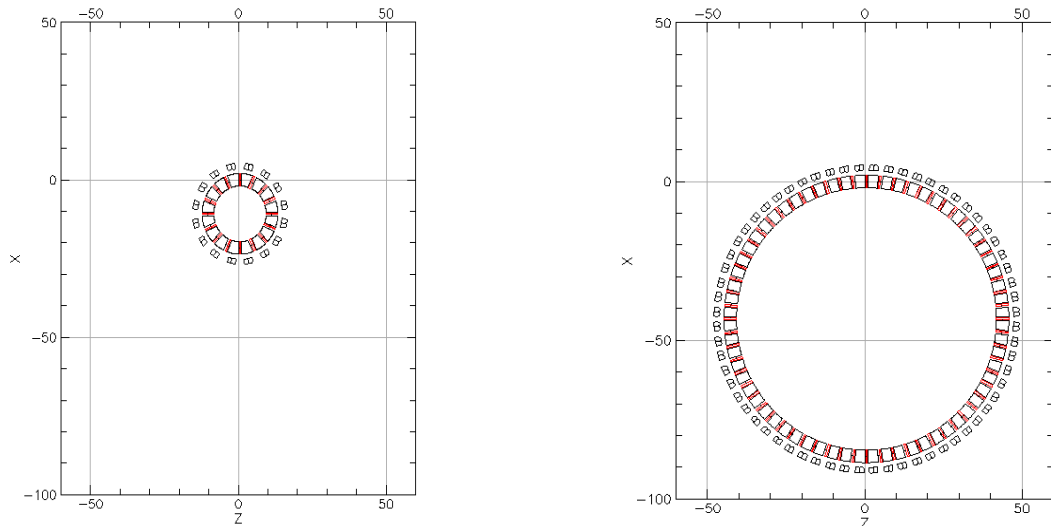


Figure 5.6: Floor plans of lattices used in this section. The small ring is displayed on the left side and the large ring is shown on the right side. Black boxes indicate the dipoles while red boxes show the quadrupoles. All axes represent the unit meter.

Apart from dipoles and quadrupoles no other elements were used in these two lattices. This should ensure that the design is as simple as possible. To have a look at the chromaticity of these two rings two approaches were chosen. The first one uses the Bmad routine *chrom_calc* which was discussed in the previous section. The second one uses equation (3.21) which just considers quadrupoles contributing to the chromaticity. The results of both approaches are shown in table (5.1).

Table 5.1: Horizontal ξ_x and vertical ξ_y chromaticities for the small and the large ring. 'Prediction (S)' uses the β -function at the beginning of a quadrupole to calculate the chromaticity and 'Prediction (E)' uses the β -function at the end of an quadrupole.

	Bmad	Prediction (S)	Prediction (E)
ξ_x, small	-0.661	-1.112	-1.181
ξ_y, small	-0.804	-1.722	-1.443
ξ_x, large	-5.596	-5.565	-5.661
ξ_y, large	-5.723	-6.052	-5.776

The chromaticity shown in the tables can be understood in the following way. The column 'Bmad' shows the results of the Bmad routine *chrom_calc*. The column 'Prediction (S)' uses the β -function at the beginning of a quadrupole to calculate the chromaticity and the column 'Prediction (E)' uses the β -function at the end of an quadrupole.

In fact the Bmad results show good agreement with the prediction of equation (3.21) in case one is facing a ring with large bending radii as one is doing in line three and four of table (5.1). The larger deviation in the vertical chromaticity $\xi_{y,large}$ is coming from the fact the vertical β -function is larger than the horizontal one.

If the ring is shrinking and the bending radii are becoming small a large disagreement between the Bmad results and the prediction results due to equation (3.21) occurs as it is shown in line one and two of table (5.1). This disagreement can only be explained with non-linear dipole contribution which are raising the chromaticity for small rings.

5.3 Chromaticity Correction

The last part of this chapter is focusing on the investigation towards working points that allow for machine operation at low sextupole strengths to correct the chromaticity which is shown in figure (5.3) and in figure (5.4). This is important as one wants to keep the impact of sextupoles on the spin motion as low as possible.

In general a sextupole is influencing horizontal and vertical chromaticity at the same time. The impact of a sextupole on the horizontal and vertical chromaticity depends on the corresponding β -function at the location of the sextupole. For this reason two new quantities are introduced which describes the ratio between horizontal and vertical β -function at exactly these locations:

$$R_{xy} = \max \left[\left(\frac{\beta_x}{\beta_y} \right) \Big|_{s=s_{\text{sextupole}}} \right] \quad (5.4)$$

$$R_{yx} = \max \left[\left(\frac{\beta_y}{\beta_x} \right) \Big|_{s=s_{\text{sextupole}}} \right]. \quad (5.5)$$

As we are facing a symmetric design consisting out of four unit cells a maximal ratio R_{xy} or R_{yx} found at one sextupole is also present at all other sextupoles of the same family. Considering a case where R_{xy} is large the corresponding sextupoles have a higher impact on the horizontal chromaticity than on the vertical one. As soon as both ratios are high enough the chromaticity can be corrected with low sextupole strengths.

To investigate this quantity the previous described scanning routine was used again. It was modified to find the maximum ratio of horizontal to vertical β -function and vice versa at the different quadrupole configurations. As the ring does have four identical unit cells a maximum which is found at one sextupole of a family is also present at all other sextupoles of this family. The results of this investigation are shown in figure (5.7) and figure (5.8).

The basic structure of these figures is identical to the structure of (5.1) and figure (5.2). In these figures the lighter blue areas indicate areas with a ratio R_{xy} or R_{yx} being lower or close to one and the darker blue areas show quadrupole configurations where the ratio R_{xy} or R_{yx} turned out to be significantly higher than one.

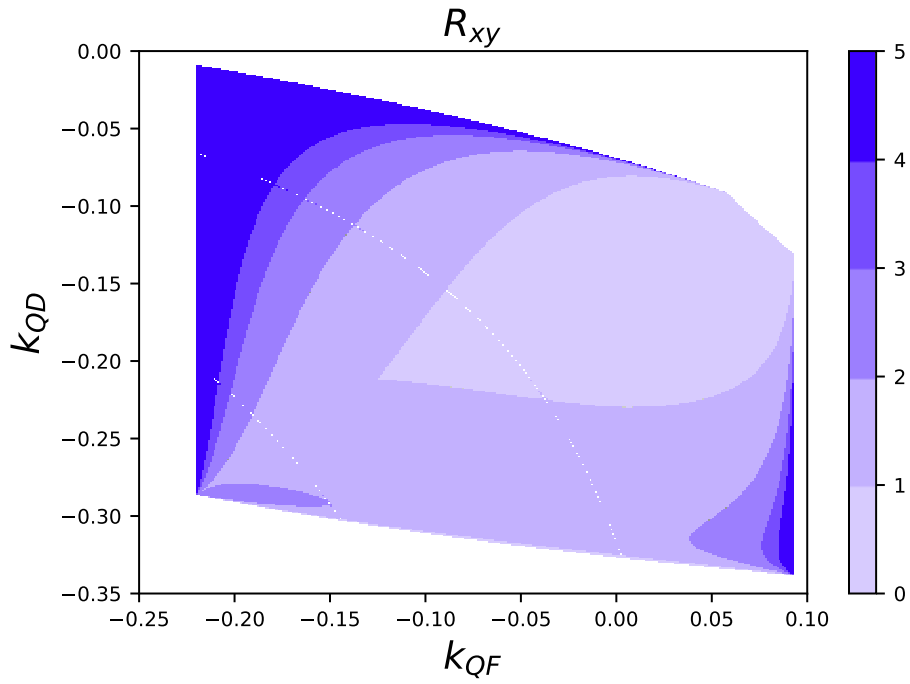


Figure 5.7: Ratio R_{xy} during the variation of the normalized quadrupole field strength k of the 'QF' and 'QD' quadrupole family. The colorbar indicates the magnitude of the ratio.

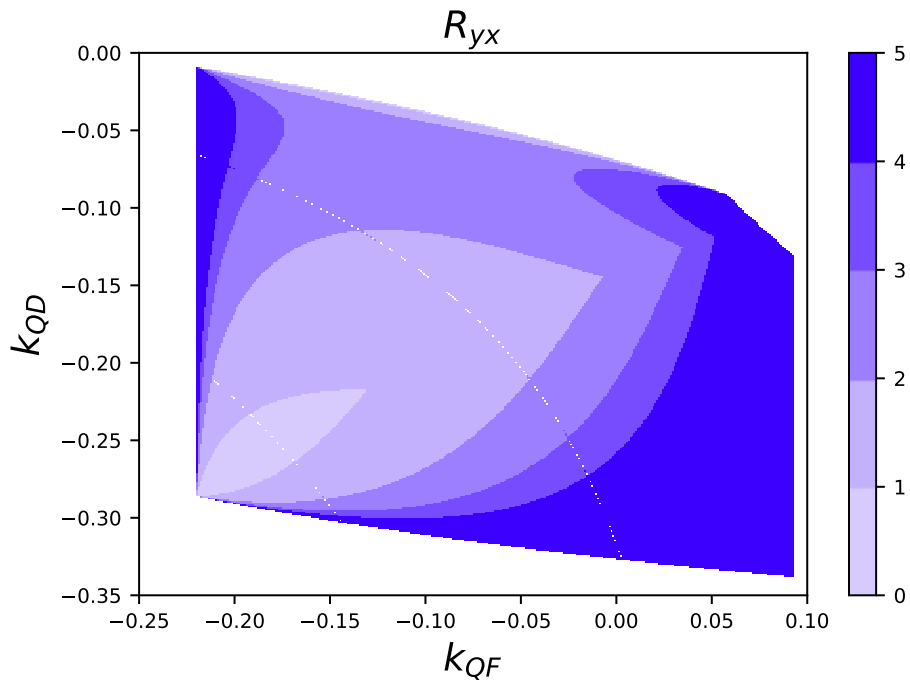


Figure 5.8: Ratio R_{yx} during the variation of the normalized quadrupole field strength k of the 'QF' and 'QD' quadrupole family. The colorbar indicates the magnitude of the ratio.

One can see that it is possible to achieve values of R_{xy} or R_{yx} which are significantly higher than one for both quantities at the same time. In the case of the prototype EDM ring this limits possible to working points to ones at the upper left side and lower right side of the area of stable operation.

If one now is looking at figure (5.3) and figure (5.4) which show then chromaticities in both planes one can see that the upper left side of the area of stable operation has high chromaticity values which have to be corrected. This is resulting in high sextupoles strengths which one wants to avoid. The lower right side of the area of stable operation is more appropriate as one has low chromaticity values of $-1 < \xi_x, \xi_y < +1$. One is also far away from strong resonances and unstable areas as it is shown in figure (5.1) and figure (5.2). Therefore the quadrupole configurations at the lower right side of the area of stable operation were chosen as a working point for performing further beam and spin tracking.

6 Investigation of Spin Motion

6.1 Preparation

6.1.1 Chosen Working Point

After discussing which criteria a possible working point should meet, the actual working point can now be determined. This working point can be used for tracking individual particles and particle beams. To investigate the SCT a particle beam has to be tracked. An explanation of the SCT is given below in section (3.4.2). There it also becomes clear why the tracking of a single particle is not sufficient for a correct determination. The properties of the chosen working point to investigate the SCT of the prototype EDM storage ring are given in table (6.1).

Table 6.1: Properties of chosen working point. The property k_{focus} shows the normalized field strength of the quadrupole family 'QF' and $k_{defocus}$ of the quadrupole family 'QD'. The horizontal betatron tune is indicated with Q_x and the vertical betatron tune with Q_y . The horizontal chromaticity is indicated with ξ_x and the vertical chromaticity with ξ_y .

k_{focus}	$k_{defocus}$	Q_x	Q_y	ξ_x	ξ_y
+0.070	-0.243	1.823	1.123	-0.070	+0.035

You can see from the table that the quadrupole family 'QF' now actually represents horizontally focusing quadrupoles, after which they were named. The same applies to the quadrupole family 'QD' which is horizontally defocusing at this working point. The working point was chosen in a way that the betatron tunes shown in column three and four of table (6.1) are far away from any betatron resonance. To demonstrate this feature the working point was drawn in a tune diagram up to third order which is shown in figure (6.1). The last two columns of the table show the natural chromaticities of the working point. As desired, these are close to zero. Figure (6.2) shows the optics of the chosen working point. Here the x-axis indicates the location inside the storage ring and the y-axis the magnitude of the individual properties which are mentioned in the legend on top of the graph. As the red dots show the locations of the quadrupoles inside the ring one can calculate the ratios R_{xy} and R_{yx} here. These results are $R_{xy} = 1.42$ and $R_{yx} = 9.32$. As the ratio R_{xy} is very low it causes higher sextupole strengths when manipulating the chromaticity in the following sections.

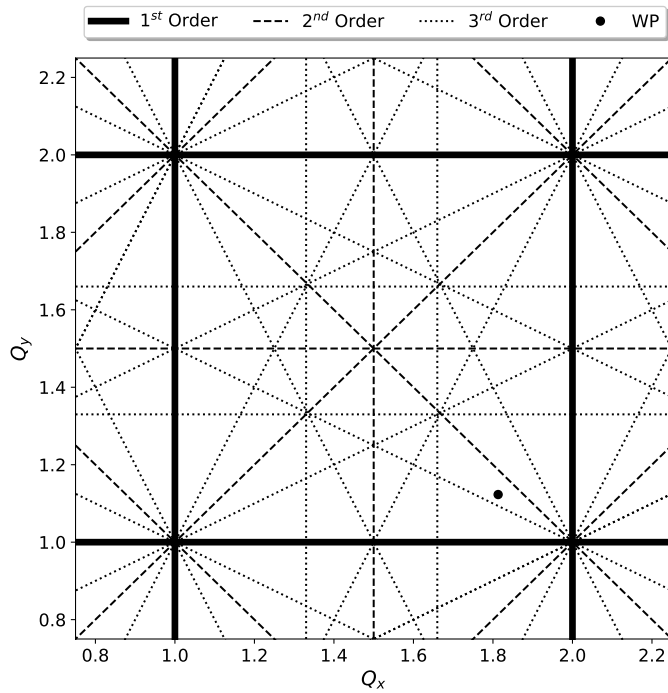


Figure 6.1: Tune diagram with resonances up to third order and chosen working point drawn inside. The x-axis shows the horizontal betatron tune Q_x and the y-axis shows the vertical betatron tune Q_y .

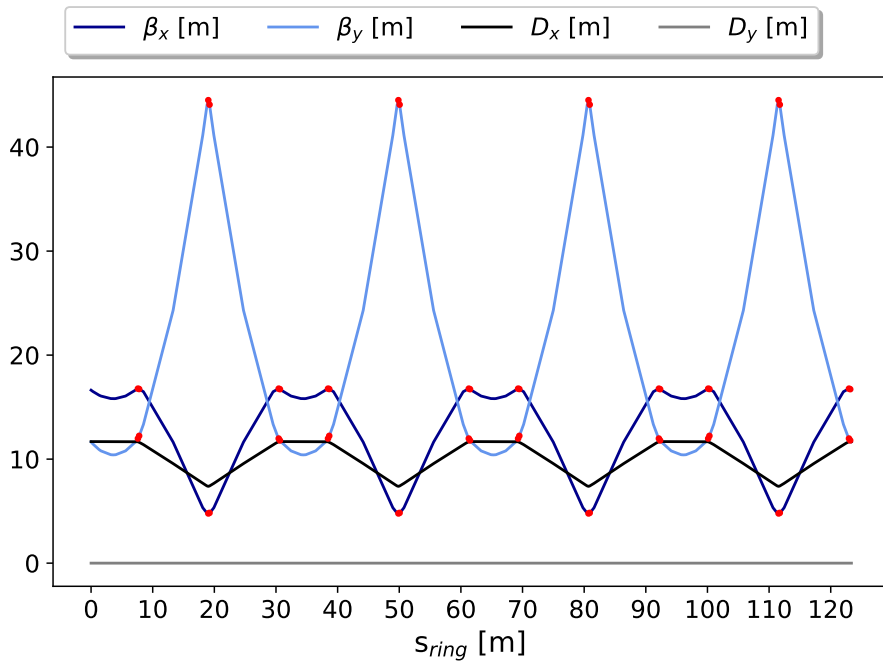


Figure 6.2: Optics of the chosen working point. The properties β_x and β_y show the horizontal and vertical β -function and D_x and D_y the horizontal and vertical dispersion. The x-axis shows the position inside the storage ring and the y-axis the magnitude of the individual properties. Location of quadrupoles are marked with red dots.

6.1.2 Initial Beam Parameter

The simulation of a multi-particle beam has been performed using two routines of the Bmad source code. These were in particular a routine to initialize a beam with predefined parameters which is called *init_beam_distribution* and a routine which is tracking the beam through the lattice named *track_beam*. The initial beam parameters are displayed in table (6.2) and (6.3).

Table 6.2: Beam Parameters.

Particle Type	Proton
Number of Particles	1000
Number of Bunches	1
Center	Closed Orbit
Beam Polarization x	0
Beam Polarization y	0
Beam Polarization z	1

Table 6.3: Beam Distribution.

x Distribution	Gaussian
y Distribution	Gaussian
z Distribution	Gaussian
ϵ_x	$5 \cdot 10^{-7} \text{ m} \cdot \text{rad}$
ϵ_y	$5 \cdot 10^{-7} \text{ m} \cdot \text{rad}$
σ_z	$1 \cdot 10^{-3}$
σ_{pz}	$1 \cdot 10^{-4}$

Table (6.2) shows that a proton beam consisting of 1000 particles in one bunch was used for the simulation. Although 1000 particles are not a realistic beam intensity, which contains approximately 10^{10} particles, this compromise between reality and simulation was chosen to avoid exceedingly long simulation times. The reference particles closed orbit was chosen to be the beam center so offset particles are moving symmetrically around the reference particles. Also a purely longitudinal polarization at the beginning of the tracking algorithm was used.

The distribution of the tracked beam are displayed in table (6.3). Since a Gaussian shape is expected from a realistic beam, this was also chosen in the simulation for the phase space coordinates. The beam emittance ϵ and the σ of the Gaussian beam distribution are connected via the β -function:

$$\epsilon_{x,y} = \frac{\sigma_{x,y}^2(s)}{\beta_{x,y}(s)}. \quad (6.1)$$

When selecting the beam distribution, care was taken to ensure that individual particles move inside the stable area of the phase space ellipse, so no particle gets lost during tracking. To check if the Bmad routine *init_beam_distribution* works properly the beam distribution after the initialization process was investigated. For this reason the phase space coordinates of every single particle of the beam were recorded. Figure (6.3) and figure (6.3) show the result of this investigation.

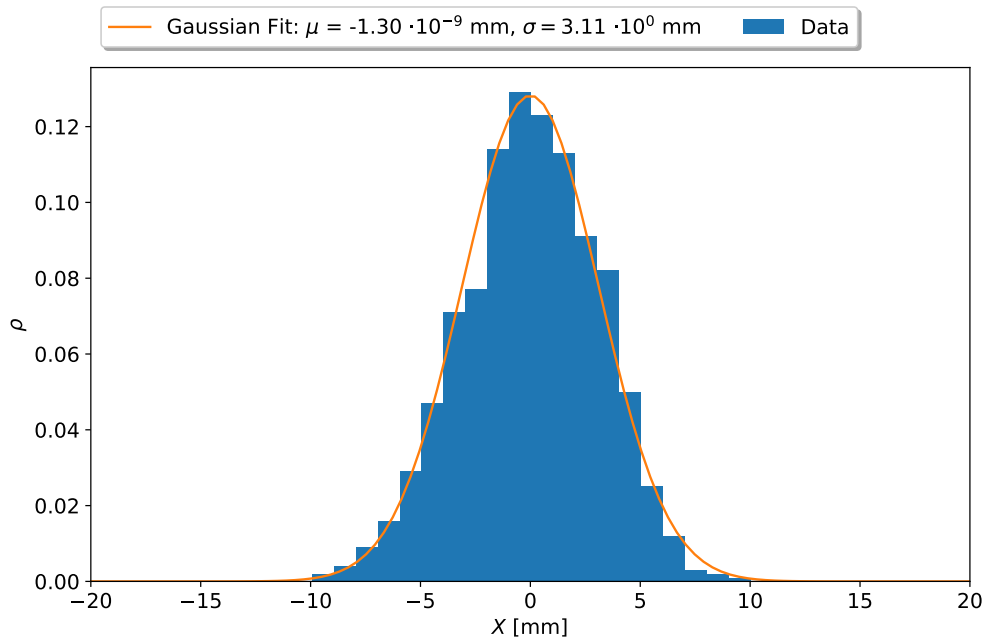


Figure 6.3: Horizontal distribution of the beam. A normalized density function is displayed on the y-axis and the deviation from the reference particle is shown on the x-axis. A Gaussian fit is indicated in orange.

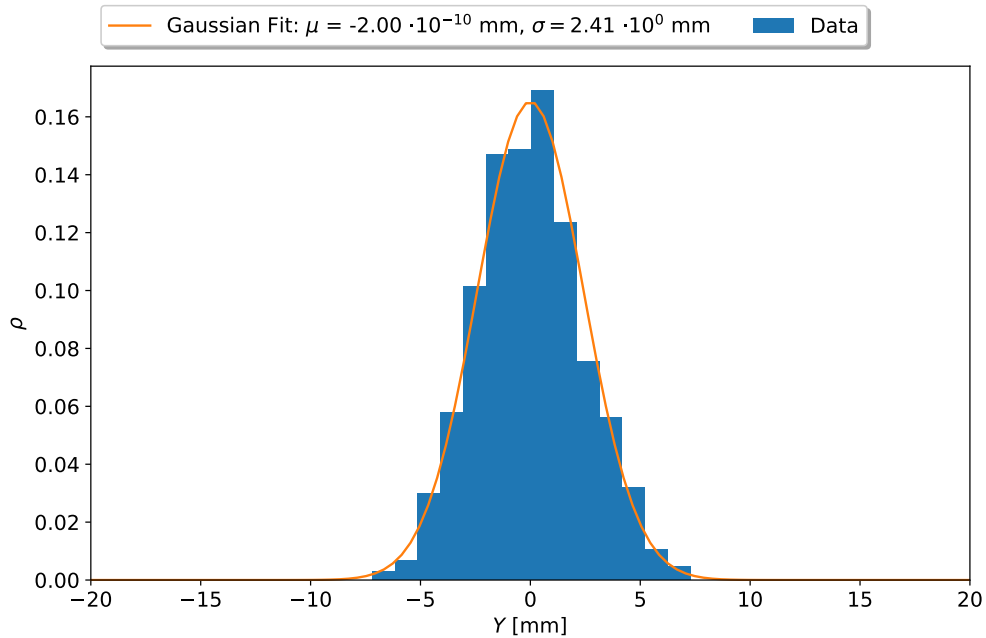


Figure 6.4: Vertical distribution of the beam. A normalized density function is displayed on the y-axis and the deviation from the reference particle is shown on the x-axis. A Gaussian fit is indicated in orange.

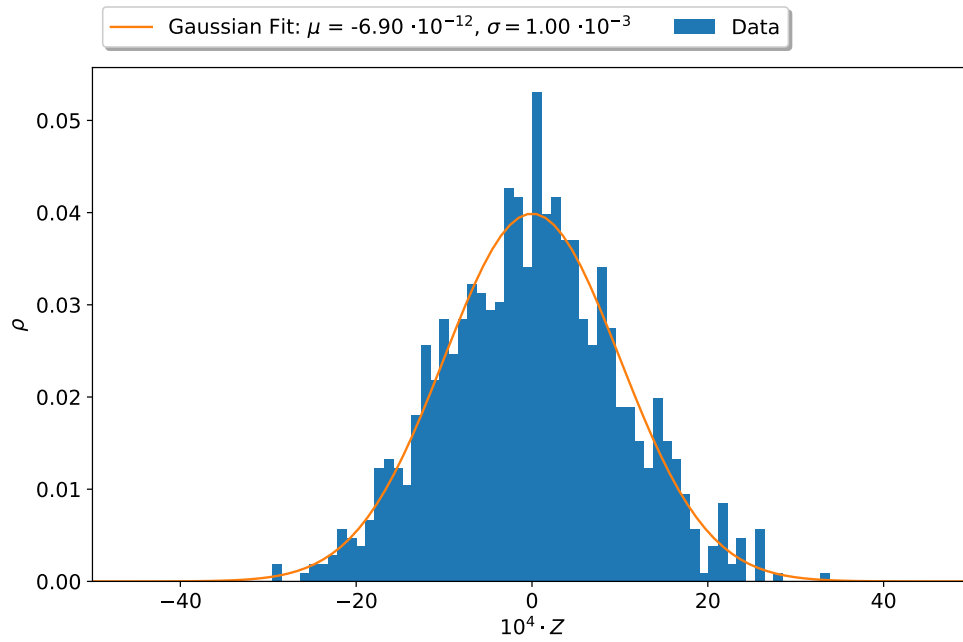


Figure 6.5: Longitudinal distribution of the beam. A normalized density function is displayed on the y-axis and the deviation from the reference particle is shown on the x-axis. A Gaussian fit is indicated in orange.

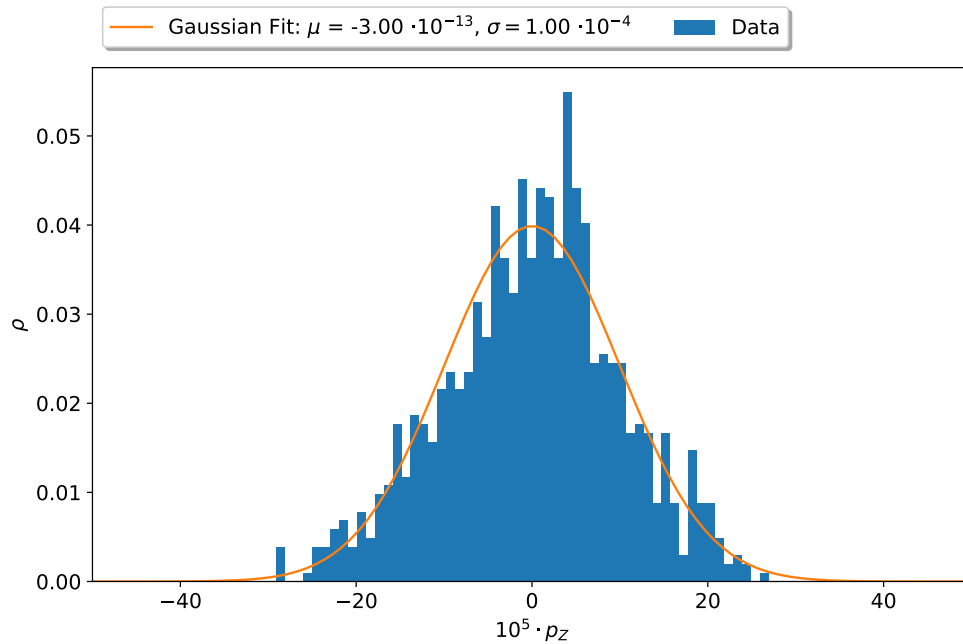


Figure 6.6: Momentum distribution of the beam. A normalized density function is displayed on the y-axis and the deviation from the reference particle is shown on the x-axis. A Gaussian fit is indicated in orange.

Figure (6.3) and (6.4) show the horizontal and vertical beam distribution at the first element of the lattice before the beam propagates through the lattice. Figure (6.5) and (6.6) show the longitudinal phase space of the beam. A Gaussian fit colored in orange indicates that the beam distribution does in fact have a Gaussian shape in all phase space coordinates. The mean μ and the standard deviation σ of the distribution are displayed above each graph.

The mean of the horizontal and vertical Gaussian distribution shows values very close to zero. As the x-axis of these plots has the unit millimeter the mean can be assumed to be zero and the visible effect is consistent with a statistical fluctuation below one σ . With equation (6.1) one is able to convert the standard deviations to emittances. The β used is the one of the lattice first element. The results read:

$$\sigma_x = 3.11 \cdot 10^{-3} \text{ m} \quad \Rightarrow \quad \epsilon_x = 5.82 \cdot 10^{-7} \text{ m} \cdot \text{rad} \quad (6.2)$$

$$\sigma_x = 2.41 \cdot 10^{-3} \text{ m} \quad \Rightarrow \quad \epsilon_x = 5.00 \cdot 10^{-7} \text{ m} \cdot \text{rad}. \quad (6.3)$$

While the emittance for the vertical phase space corresponds to the parameter used in the routine *init_beam_distribution*, this does not apply to the horizontal phase space. The reason for this is the fact that horizontal and longitudinal phase space are coupled. As a momentum deviation inside beam is introduced the horizontal emittance is increasing. In case the momentum deviation is not considered and chosen to be zero also the result for the horizontal emittance corresponds to the parameter used in the routine *init_beam_distribution*.

If one is looking at the mean for the longitudinal phase space the case is quite similar to the horizontal and vertical phase space coordinates. The reason that the means deviate from zero is statistical fluctuation. The standard deviation here is in perfect agreement with the ones used as a parameter in the routine *init_beam_distribution*.

This shows that the previously defined beam parameters were transferred to the simulation program as desired. Calling the function *track_beam* leads to the propagation of the beam through the lattice. In this simulation no interaction between the protons inside the particle beam was considered. For this reason a single particle in the particle beam behaves identically to a single tracked particle.

6.2 Variation of vertical Chromaticity

To optimize the SCT at a given working point the chromaticity can be varied. This can be achieved by the manipulation of the sextupoles strengths. To keep the approach as simple as possible the horizontal chromaticity is kept at a value of zero while the vertical chromaticity is manipulated. The sextupole strengths needed to achieve the desired horizontal and vertical chromaticities are shown in table (6.4).

Table 6.4: Sextupole strengths needed for chromaticity manipulation. The properties $\xi_{x,des}$ and $\xi_{y,des}$ show the desired horizontal and vertical chromaticities and the properties $k_{2,SXF}$ and $k_{2,SXD}$ the normalized sextupole field strengths to achieve those. The indices at these properties show if they belong to the sextupole family 'SXF' or 'SXD'.

$\xi_{x,des}$	$\xi_{y,des}$	$k_{2,SXF} [1/m^3]$	$k_{2,SXD} [1/m^3]$
0	-10	-0.022	+0.259
0	-08	-0.017	+0.207
0	-06	-0.013	+0.155
0	-04	-0.008	+0.104
0	-02	-0.003	+0.052
0	0	+0.001	± 0.000
0	+02	+0.006	-0.052
0	+04	+0.011	-0.104
0	+06	+0.015	-0.156

Here the first column shows the desired horizontal chromaticity while the second column shows the desired vertical chromaticity. The actual chromaticity values $\xi_{x,act}$ and $\xi_{y,act}$ are able to differ from the desired value $\xi_{x,des}$ and $\xi_{y,des}$. This difference ϵ_{chrom} is described in equation (6.4) and was set to stay below 0.01 in order to ensure that the desired chromaticity values are in good agreement with the actual ones:

$$\epsilon_{chrom} = |\xi_{x,act} - \xi_{x,des}| + |\xi_{y,act} - \xi_{y,des}|. \quad (6.4)$$

The third column of table (6.4) shows the strengths of the sextupoles placed on the quadrupole family 'QF' and the last column the strengths of the sextupoles placed on the quadrupole family 'QD'. Being able to tune the chromaticities to the desired values the SCT and the spin tune spread can be investigated. This was done by recording the spherical spin polarization at the beginning of each turn. The beam used for this investigation had the properties mentioned in the sections before. The result for a configuration of zero horizontal and zero vertical chromaticity is shown in figure (6.7) as an example.

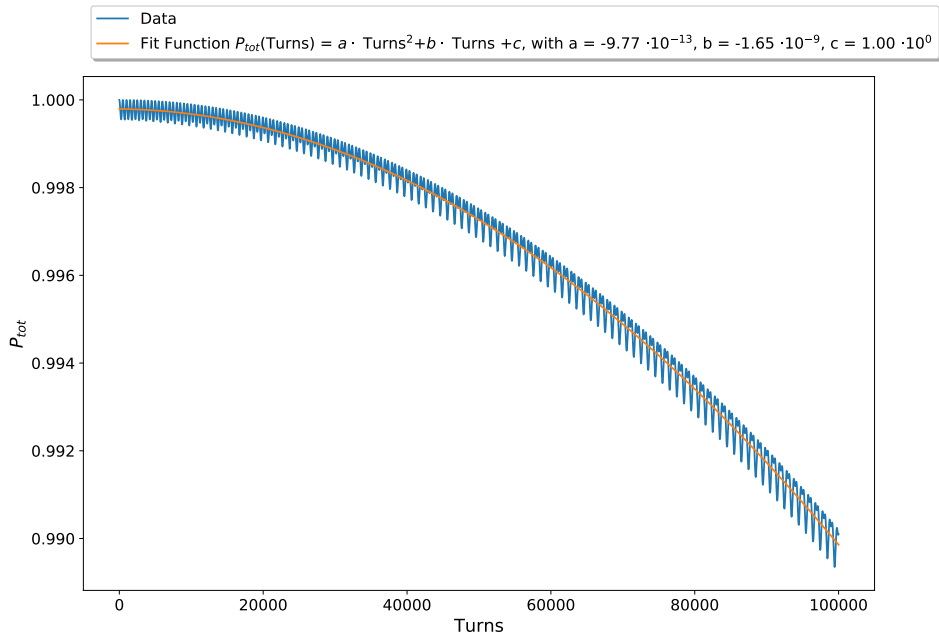


Figure 6.7: Evolution of total spin polarization P_{tot} during 100000 turns. A quadratic fit to the simulation data is indicated in orange. Exemplary plot for a chromaticity configuration of $\xi_x = 0$ and $\xi_y = 0$.

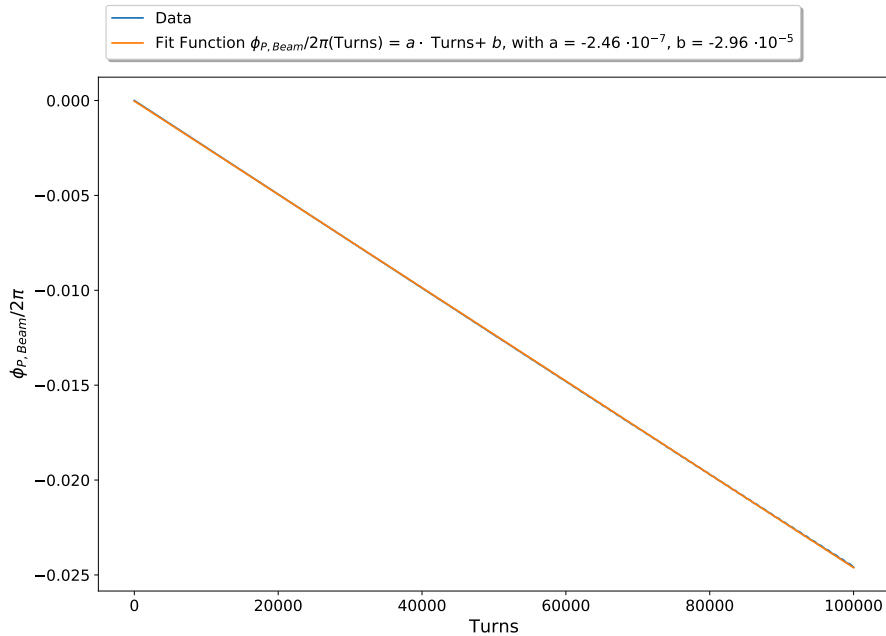


Figure 6.8: Evolution of horizontal polarization orientation $\phi_{P,Beam}$ during 100000 turns. A linear fit drawn in orange covers the blue data points. Exemplary plot for a chromaticity configuration of $\xi_x = 0$ and $\xi_y = 0$.

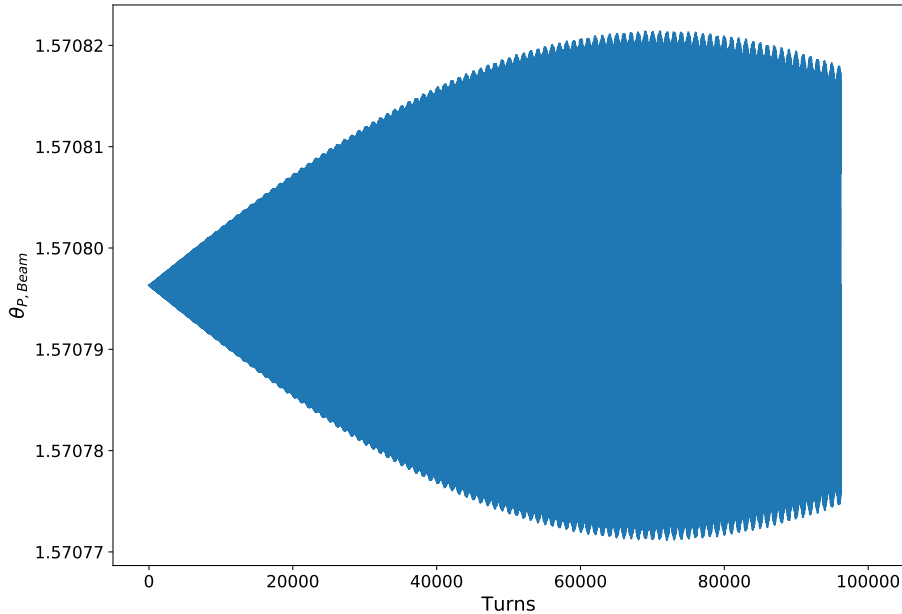


Figure 6.9: Evolution of vertical polarization orientation $\theta_{P,Beam}$ during 100000 turns. The initial angular $\theta_{P,Beam}$ corresponds to $\pi/2$. Exemplary plot for a chromaticity configuration of $\xi_x = 0$ and $\xi_y = 0$.

The three exemplary plots above show the evolution of the spherical spin polarization. The x-axis indicates the number of turns the beam already propagated and the y-axis denotes the magnitude of the corresponding spherical spin polarization.

In the first plot which shows the total spin polarization a quadratic fit to the blue data points was performed which is indicated in orange. The assumption of a quadratic behavior is reasonable as one would expect a damped oscillation of the total spin. As this damped oscillation behaves like a cosine function a quadratic fit is appropriate. Using the parameters of the quadratic fit shown in figure (6.7) an estimation of the SCT could be made. The second plot, figure (6.8), shows the rotation of the horizontal spin polarization. As this is directly connected to the spin tune spread as shown in equation (3.54) a linear fit was performed this figure which is indicated in orange. This linear fit covers the blue data points. As the reference particles spin is frozen ($\phi_s = 0$) the slope of the linear fit reveals the spin tune spread $\Delta\nu_s$. The last plot, figure (6.9), shows the vertical spin build up. The initial angular of $\theta_{P,Beam}$ corresponds to $\pi/2$ which indicates no vertical spin build up. During the propagation of the beam through the lattice it deviates from its starting value of $\pi/2$. It can be shown that these small symmetric deviations are induced by the vertical distribution of the beam. If the vertical distribution is turned of no deviation is visible.

The estimation of the SCT and the spin tune spread was obtained for every sextupole configuration mentioned in table (6.4). The results are shown in the figure (6.10) and figure (6.11). The first figure shows the SCT on the y-axis and the vertical chromaticity on the x-axis. The data points are displayed in blue and a Gaussian fit to the data points is indicated in orange.

In the second figure the y-axis shows the spin tune spread while the x-axis displays the vertical chromaticity. Here the data points are also colored blue while a linear fit is performed in orange. In both figures the fitting parameters are displayed in the legend above. The errors of each data point are obtained from the quadratic and linear fit before. They are so small that they become invisible in these graphs.

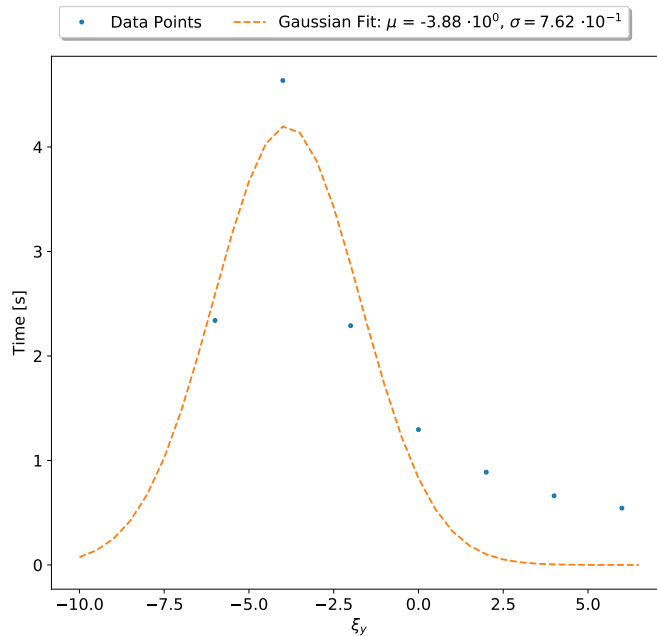


Figure 6.10: SCT for a particle beam consisting of 1000 particles versus vertical chromaticity ξ_y . The horizontal chromaticity ξ_x is set to zero while the vertical chromaticity ξ_y is varied along the x-axis. A Gaussian fit to the data is indicated in orange.

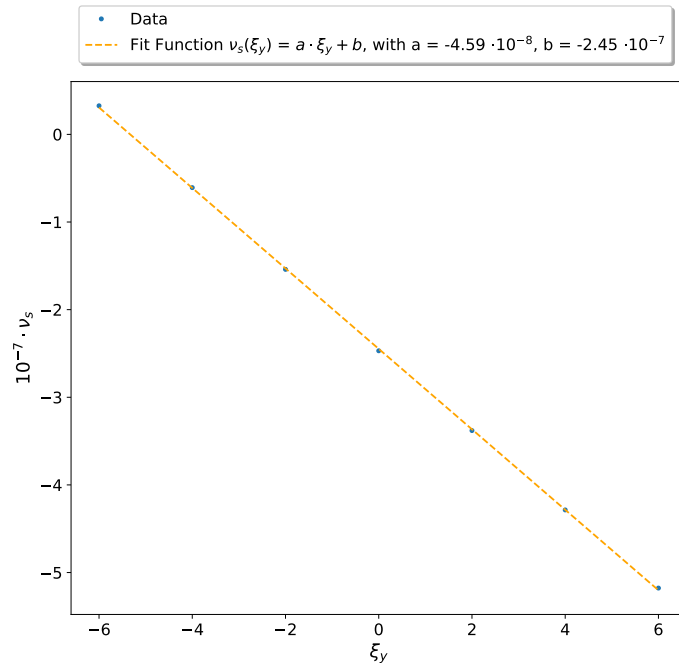


Figure 6.11: Spin tune spread ν_s for a particle beam consisting of 1000 particles versus vertical chromaticity ξ_y . The horizontal chromaticity ξ_x is set to zero while the vertical chromaticity ξ_y is varied along the x-axis. A linear fit to the data is indicated in orange.

In figure (6.10) one can see from the fitting parameters that the longest SCT is achieved at a vertical chromaticity of $\xi_y = -3.88$. Naively one would expect, that the longest spin coherence time is achieved at the same chromaticity configuration at which the spin tune spread is minimal. The minimal spin tune spread can be calculated by the linear fit in figure (6.11). The result is that the minimal spin tune spread is achieved at a vertical chromaticity of $\xi_y = -5.33$.

This is a surprising result and one might explain it with the missing data points on the falling flank of the Gaussian distribution. The SCT and the spin tune spread was therefore re-investigated with only 100 particle and compared with the result for 1000 particles. The results are shown in figure (6.13) and figure (6.13). Their individual quantities are displayed on the y-axis and the vertical chromaticities on the x-axis. The data points are shown in blue while the fits are marked with orange.

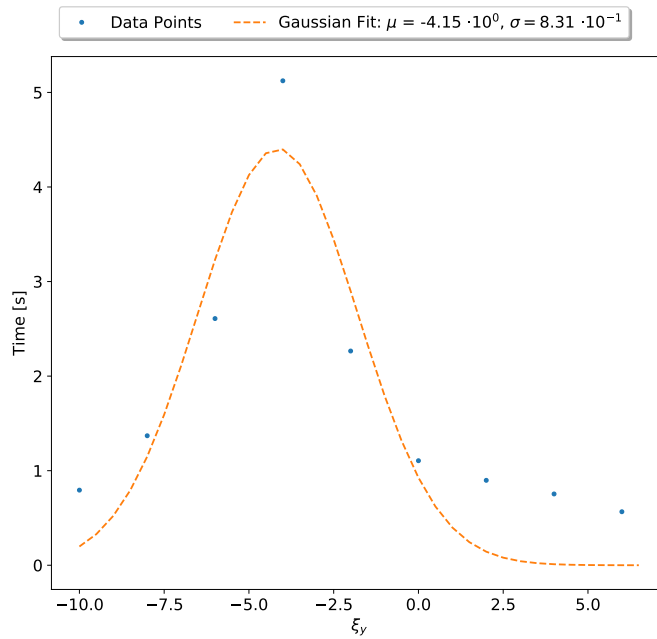


Figure 6.12: SCT for a particle beam consisting of 100 particles versus vertical chromaticity ξ_y . The horizontal chromaticity ξ_x is set to zero while the vertical chromaticity ξ_y is varied along the x-axis. A Gaussian fit to the data is indicated in orange.

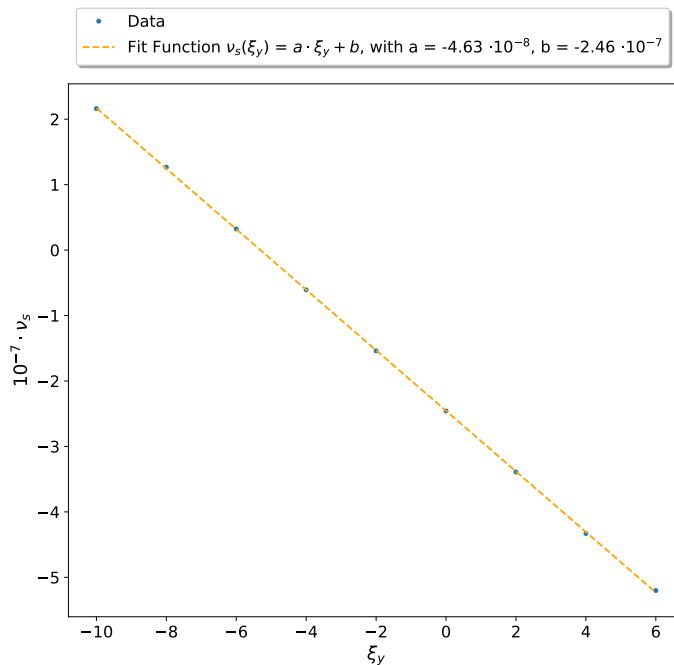


Figure 6.13: Spin tune spread ν_s for a particle beam consisting of 100 particles versus vertical chromaticity ξ_y . The horizontal chromaticity ξ_x is set to zero while the vertical chromaticity ξ_y is varied along the x-axis. A linear fit to the data is indicated in orange.

It is remarkable that the results for 1000 particles and 100 particles are similar. The minimal spin tune spread is at $\xi_y = -5.33$ for 1000 and $\xi_y = -5.31$ for 100 particles which indicates that one would expect the maximum SCT at the same vertical chromaticity for 100 and 1000 particles. This is not the case as the Gaussian fit shows that it is at $\xi_y = -3.88$ for 1000 and $\xi_y = -4.15$ for 100 particles.

This disagreement between the results for 100 and 1000 particles can be explained with the missing data points on the falling flank of the Gaussian fit for 1000 particles. What the missing data points are not explaining is the disagreement between the longest SCT and the minimal spin tune spread. The longest SCT and the minimal spin tune spread are still more than one σ away from each other.

A possible explanation for the mismatch is the fact that spins axis of rotation in phase space was assumed to be vertical. In the vicinity of spin resonances this axis can drop. The determination of this axis can be performed by the so-called stroboscopic averaging. This has not been considered here, but can have an influence and explain the discrepancy between longest SCT and minimum spin tune spread [28].

In a previous investigation on the purely magnetic storage ring COSY with deuterons it was already shown that the minimal spin tune spread can be described by the following formula [29]:

$$0 = |A + a_1 I_S + a_2 I_L + a_3 I_G| \langle x'^2 \rangle + |B + b_1 I_S + b_2 I_L + b_3 I_G| \langle y'^2 \rangle + O(\langle (\Delta p/p)^2 \rangle) \quad (6.5)$$

In this formula the parameter A and B represent the contribution of the natural chromaticity of the ring, while I_S , I_L and I_G show the currents applied to the three sextupole groups located in the arcs of COSY. The coefficients a_i and b_i define the sensitivity of the beam properties to the sextupole strengths. A term proportional to $\langle (\Delta p/p)^2 \rangle$ arises due to the synchrotron motion. This formula suggests that in case of zero chromaticity the first and second term vanishes and the spin tune spread becomes close to zero. This would result in the maximum SCT [29].

The investigation actually shows that there are sextupole configurations inside COSY at which the SCT becomes very long. An independent measurement during the same project shows that these sextupole configurations coincide with almost zero chromaticity. This can be explained by the fact that all particle paths have the same length regardless of their betatron oscillation [29].

The question arises why the results presented in this thesis deviate from this results. In contrast to the previous mentioned investigation of the longest SCT and minimal spin tune spread do not appear at a chromaticity of zero in both planes. Furthermore, the maximum SCT and the minimum spin tune spread are not at the same sextupole configuration. However, it should be noted, that the COSY and the prototype EDM storage ring behave in an elementary different way with respect to the spin motion.

This is shown by the fact that COSY is a purely magnetic ring and thus the spin of the reference particle oscillates. In contrast, the prototype EDM storage ring allows the spin of the reference particle to be frozen. Also the fields a particle experiences are different as the prototype EDM storage ring provides an additional electric field to the magnetic field inside the dipoles. Furthermore, the measurements at COSY used deuterons while protons were used in this work.

At this stage it is not possible to clearly explain why the optimal SCT of both rings is so different. This can only be done once the spin motion of a particle in the prototype EDM storage ring is better understood.

7 Summary and Outlook

To perform a high-precision experiment to determine the EDM of a charged particle at a storage ring one needs an exact understanding of the spin motion. This thesis is focusing on the simulation of such a spin motion in the so-called prototype EDM storage ring. Its special feature is to have bending dipoles with combined magnetic and electric fields which keep the spin of the reference particle aligned with its momentum.

An idealized model of the prototype EDM storage ring design from February 2020 was used and benchmarked within this thesis. No misalignments or field errors were considered. An investigation of possible working points has been performed by varying the quadrupole strengths. The evaluation of this investigation shows that one is able to achieve horizontal and vertical betatron tunes in between the range of zero and two. For tune values higher than two no stable solution could be determined. In parallel the chromaticity of the working points was recorded which varies widely and even changes its sign. It has been found out and shown that this is a natural behavior for small storage rings.

Using sextupoles being mounted right on top of the quadrupoles to manipulate the chromaticity, the dependency of the spin coherence time and the spin tune spread on chromaticity was investigated. It was observed that the optimum values for the maximal SCT and minimal spin tune spread do not coincide. The reason for this could be the fact that stroboscopic averaging has to be taken into account to determine the spins axis of rotation. Also maximal SCT and minimal spin tune spread deviate from zero chromaticity in both planes. This observation could not be explained in the course of this work.

In the future, this observation must be further investigated and verified. For this reason, one first has to switch from the lattice of the prototype EDM ring back to the COSY lattice, since here the spin motion is already better understood and simulation results can be compared with measurement results. As soon as one achieves an agreement between simulation and measurement, one can work back from the COSY model to the prototype EDM storage ring.

In conclusion, this work has shown how to model an electromagnetic dipole in Bmad. Furthermore, the flexibility of the lattice with respect to betatron tunes and natural chromaticity was investigated. Finally, it was shown that the SCT behaves differently than expected under the influence of electric fields.

8 Appendix

Table 8.1: Parameters of an electromagnetic sector dipole in Bmad [24].

Attribute	Parameter Name	Input
Field Type	fringe_type	basic_bend
Length	l	dipole_length
Curvature	b_field	geometric_b_field
Magnetic Field	b_field_err	actual_b_field - geometric_b_field
Electric Field	b0_elec	-actual_e_field

List of Figures

3.1	Sketch of co-moving coordinate system.	5
3.2	Horizontal phase space ellipse.	9
3.3	Tune diagram with betatron resonances up to third order.	11
3.4	Sketch of the principle of chromaticity correction by sextupoles.	13
3.5	Principle of phase focusing.	16
3.6	Sketch of spin rotation due to magnetic and electric fields.	20
3.7	Polarization Transformation.	23
4.1	Layout of a unit cell.	26
4.2	Basic layout of the prototype EDM storage ring.	27
4.3	Floor plan of the prototype EDM ring made with the Tao module.	29
4.4	Closed orbit and momentum deviation of the storage ring.	31
4.5	Evolution of phase space for a particle starting on the closed orbit.	32
4.6	Electric and magnetic field inside the dipoles.	33
4.7	Evolution of spin for a particle starting on the closed orbit.	34
4.8	Phase space ellipses at two different locations.	35
5.1	Scan horizontal betatron tune.	38
5.2	Scan vertical betatron tune.	38
5.3	Scan of horizontal chromaticity.	41
5.4	Scan of vertical chromaticity.	41
5.5	Layout of a unit cell.	43
5.6	Floor plans of two test lattices.	43
5.7	Scan of ratio R_{xy}	46
5.8	Scan of ratio R_{yx}	46
6.1	Tune diagram with chosen working point drawn inside.	50
6.2	Optics of the chosen working point.	50
6.3	Horizontal distribution of the beam.	52
6.4	Vertical distribution of the beam.	52
6.5	Longitudinal distribution of the beam.	53
6.6	Momentum distribution of the beam.	53
6.7	Evolution of total spin polarization P_{tot}	56
6.8	Evolution of horizontal polarization $\phi_{P,Beam}$ orientation.	56
6.9	Evolution of vertical polarization orientation $\theta_{P,Beam}$	57

6.10	SCT versus vertical chromaticity ξ_y for 1000 particles.	58
6.11	Spin tune spread ν_s versus vertical chromaticity ξ_y for 1000 particles.	59
6.12	SCT versus vertical chromaticity ξ_y for 100 particles.	60
6.13	Spin tune spread ν_s versus vertical chromaticity ξ_y for 100 particles.	60

List of Tables

2.1	Current upper limits of EDM searches.	4
3.1	Magnetic properties of proton, electron and deuteron.	18
3.2	Summary of depolarizing spin resonances.	23
4.1	Summary of important features of proposed stages.	26
4.2	Summary of lattice elements.	27
4.3	Kinematic parameters of reference particle.	27
5.1	Chromaticities for the small and the large test rings.	44
6.1	Properties of chosen working point.	49
6.2	Beam Parameters.	51
6.3	Beam Distribution.	51
6.4	Sextupole strengths needed for chromaticity manipulation.	55
8.1	Parameters of an electromagnetic sector dipole in Bmad.	i

Bibliography

- [1] I. B. Khriplovich and S. K. Lamoreaux, *CP Violation Without Strangeness: Electric Dipole Moments of Particles, Atoms, and Molecules*, Springer Berlin Heidelberg, ISBN 978-3-642-60838-4, 1997.

- [2] JEDI Collaboration, *Search for Permanent Electric Dipole Moments at COSY*, 2014.
http://collaborations.fz-juelich.de/ikp/jedi/public_files/proposals/JEDI-COSY-PROPOSAL-FINAL_21.1.2014.pdf [07.09.2020]

- [3] A. Lehrach, S. Martin and R. Talman, *Design of a Prototype EDM Storage Ring*, Proceedings of Science, PoS SPIN2018, 144, 2018.
http://collaborations.fz-juelich.de/ikp/jedi/public_files/proceedings/Spin2018_EDM_AL.pdf [07.09.2020]

- [4] A. Wirzba, *Electric dipole moments of the nucleon and light nuclei*, Nuclear Physics A 928, pp. 116-127, 2014.
<https://arxiv.org/pdf/1404.6131.pdf> [07.09.2020]

- [5] C. L. Bennett et al., *Nine-Year Wilkinson Microwave Anisotropy Probe (WMAP) Observations: Final Maps and Results*, The Astrophysical Journal Supplement Series 208, 2013.
<https://arxiv.org/pdf/1212.5225v1.pdf> [07.09.2020]

- [6] W. Bernreuther, *CP Violation and Baryogenesis*, Lecture Notes in Physics, Springer, ISBN 978-3-540-47895-9, pp. 237-293, 2002.
<https://arxiv.org/pdf/hep-ph/0205279.pdf> [07.09.2020]

- [7] A. D. Sakharov, *Violation of CP Invariance, C Asymmetry, and Baryon Asymmetry of the Universe*, Pisma Zh. Eksp. Teor. Fiz., pp. 32– 35, 1967.

- [8] T. Fukuyama and A. J. Silenko, *Derivation of Generalized Thomas-Bargmann-Michel-Telegdi Equation for a Particle with Electric Dipole Moment*, International Journal of Modern Physics A28, 1350147, 2013.
<https://arxiv.org/pdf/1308.1580.pdf> [07.09.2020]

-
- [9] M. Rosenthal, *Experimental Benchmarking of Spin Tracking Algorithms for Electric Dipole Moment Searches at the Cooler Synchrotron COSY*, PhD Thesis, RWTH Aachen University, 2016.
http://collaborations.fz-juelich.de/ikp/jedi/public_files/theses/Thesis_MRosenthal.pdf [07.09.2020]
- [10] F. Rathmann, *Search for permanent Electric Dipole Moments of light ions (p , d , ${}^3\text{He}$) in storage rings*, 2012.
http://collaborations.fz-juelich.de/ikp/jedi/public_files/proposals/merged_document.pdf [07.09.2020]
- [11] W. Dekens and J. de Vries, *Renormalization Group Running of Dimension-Six Sources of Parity and Time-Reversal Violation*, Journal of High Energy Physics, 2013.
<https://arxiv.org/pdf/1303.3156.pdf> [10.09.2020]
- [12] C. A. Baker et al., *An Improved Experimental Limit on the Electric Dipole Moment of the Neutron*, Physical Review Letters 97, 131801, 2006.
<https://arxiv.org/pdf/hep-ex/0602020.pdf> [07.09.2020]
- [13] W. C. Griffith, M. D. Swallows and T. H. Loftus et al., *Improved Limit on the Permanent Electric Dipole Moment of ${}^{199}\text{Hg}$* , Physical Review Letters 102, 101601, 2009.
<https://arxiv.org/pdf/0901.2328.pdf> [07.09.2020]
- [14] ACME Collaboration, *Order of Magnitude Smaller Limit on the Electric Dipole Moment of the Electron*, Science Volume 343, pp. 269-272, 2014.
<https://arxiv.org/pdf/1310.7534.pdf> [07.09.2020]
- [15] K. Wille, *Physik der Teilchenbeschleuniger und Synchrotronstrahlungsquellen*, Springer Fachmedien Wiesbaden, ISBN 978-3-663-11850-3, 1996.
- [16] H. Wiedemann, *Particle Accelerator Physics*, Springer International Publishing, ISBN 978-3-319-18317-6, 2014.
- [17] S. Y. Lee, *Spin Dynamics and Snakes in Synchrotrons*, World Scientific, ISBN 978-981-3105-01-0, 1997.
- [18] National Institut of Standards and Technology.
<https://physics.nist.gov/cuu/Constants/index.html> [11.08.2020]
- [19] V. Hejny, *Measurement of Electric Dipole Moments at Storage Rings*, Hadron Physics Summer School, 2018.
http://collaborations.fz-juelich.de/ikp/jedi/public_files/usual_event/hpss2018-EDM-web.pdf [10.09.2020]
-

-
- [20] J. Pretz, *Measurement of permanent electric dipole moments of charged hadrons in storage rings*, *Hyperfine Interactions*, Volume 214, Issue 1-3 , pp. 111-117, 2013.
<https://arxiv.org/pdf/1301.2937.pdf> [07.09.2020]
- [21] A. A. Skawran, *Comparison of Frozen and Quasi Frozen Spin Concepts for a Deuteron Electrical Dipole Moment Storage Ring*, Master Thesis, RWTH Aachen University, 2016.
http://collaborations.fz-juelich.de/ikp/jedi/public_files/theses/Thesis-final.pdf [07.09.2020]
- [22] JEDI Collaboration.
<http://collaborations.fz-juelich.de/ikp/jedi/> [11.08.2020]
- [23] Charged Particle Electric Dipole Moment Collaboration, *Feasibility Study for an EDM Storage Ring*, 2018.
<https://arxiv.org/pdf/1812.08535.pdf> [07.09.2020]
- [24] D. C. Sagan, *The Bmad Reference Manual*, 2019.
<https://www.classe.cornell.edu/bmad/manual.html> [25.08.2020]
- [25] D. C. Sagan, *The Tao Manual*, 2019.
<https://www.classe.cornell.edu/bmad/tao.html> [25.08.2020]
- [26] S. Martin, Forschungszentrum Jülich, Private Communication.
- [27] A. J. Dragt, *Exact Numerical Calculation of Chromaticity in Small Rings*, *Particle Accelerators*, Volume 12, pp. 205-218, 1982.
<https://cds.cern.ch/record/890994/files/p205.pdf> [07.09.2020]
- [28] K. Heinemann and G. H. Hoffstätter, *Tracking algorithm for the stable spin polarization field in storage rings using stroboscopic averaging* , *Physical Review E*, Volume 54, pp. 4240–4255, 1996.
<https://arxiv.org/pdf/acc-phys/9605001.pdf> [14.09.2020]
- [29] G. Guidoboni et al., *Connection between zero chromaticity and long in-plane polarization lifetime in a magnetic storage ring*, *Physical Review Accelerators and Beams* 21, 024201, 2018.
<https://journals.aps.org/prab/pdf/10.1103/PhysRevAccelBeams.21.024201>
[07.09.2020]

Acknowledgments

First of all I would like to give my sincere gratitude to Prof. Dr. Andreas Lehrach for giving me the opportunity to write this thesis. He introduced me into the fascinating field of accelerator physics and was always willing to offer support in technical issues.

I would like to thank Prof. Dr. Anke Schmeink for acceding to be the second supervisor of this work.

A special thanks to Vera Poncza for all her advice and patience in the last year. Even after she had already left the institute, she still had time for me and continued to support me.

Another big thanks I want to say to David Sagan, who always gave me support regarding Bmad.

I would also like to thank the members of the JEDI collaboration for the discussions before, during and after our meetings.

Finally I would like to thank my girlfriend for supporting me during the last year. All I had to worry about was physics.

Eidesstattliche Versicherung

Vitz, Maximilian

332024

Name, Vorname

Matrikelnummer

Ich versichere hiermit an Eides Statt, dass ich die vorliegende Masterarbeit mit dem Titel **Simulation and Optimization of the Spin Coherence Time of Protons in a Prototype EDM Ring**

selbständig und ohne zulässige fremde Hilfe erbracht habe. Ich habe keine anderen als die angegebenen Quellen und Hilfsmittel benutzt. Für den Fall, dass die Arbeit zusätzlich auf einem Datenträger eingereicht wird, erkläre ich, dass die schriftliche und die elektronische Form vollständig übereinstimmen. Die Arbeit hat in gleicher oder ähnlicher Form noch keiner Prüfungsbehörde vorgelegen.

Aachen, 20. Oktober 2020

Ort, Datum

Unterschrift